Interaction of equal-size bubbles in shear flow

Jai Prakash,[*] Olga M. Lavrenteva,[†] Leonid Byk, and Avinoam Nir[‡]
Department of Chemical Engineering
Technion—Israel Institute of Technology, Haifa 32000, Israel
(Received 4 December 2012; revised manuscript received 11 February 2013; published 8 April 2013)

The inertia-induced forces on two identical spherical bubbles in a simple shear flow at small but finite Reynolds number, for the case when the bubbles are within each other's inner viscous region, are calculated making use of the reciprocal theorem. This interaction force is further employed to model the dynamics of air bubbles injected to a viscous fluid sheared in a Couette device at the first shear flow instability where the bubbles are trapped inside the stable Taylor vortex. It was shown that, during a long time scale, the inertial interaction between the bubbles in the primary shear flow drives them away from each other and, as a result, equal-size bubbles eventually assume an ordered string with equal separation distances between all neighbors. We report on experiments showing the dynamic evolution of various numbers of bubbles. The results of the theory are in good agreement with the experimental observations.

DOI: 10.1103/PhysRevE.87.043002 PACS number(s): 47.32.Ef, 47.55.dd

I. INTRODUCTION

Interaction of suspended bubbles with the flow and with other bubbles is an important issue for many natural and technological processes. Bubbles suspended in a quiescent liquid tend to rise due to buoyancy. However, in intensive flow, bubbles exhibit complicated behavior, e.g., they may be trapped by vortices. Djéridi *et al*. [1,2] performed experimental study of bubbles capture and migration in a Couette-Taylor flow at Reynolds numbers, corresponding to the first classical instabilities of the flow. The study of Deng *et al*. [3] is focused on the behavior of individual bubbles embedded in such flow. It was demonstrated that the bubbles are trapped either near the wall at stagnation points or in the vortex core. Equal-size bubbles entrapped in the core eventually assume an ordered string with equal separation distances between all neighbors. Thus, doublets assume opposite positions, triplets will form a triangle, four bubbles will arrange in a square, and so on. This phenomenon repeats itself with the introduction of additional bubbles to the flow up to a certain number. Experiments performed in our laboratory reproduce these results and also provide detailed measurements of the process evolution. A brief report of these results can be found in Byk *et al*. [4] and more details are presented in the present paper. Thus, the equilibrium configurations for 2, 3, 4, 5, 12, and 14 bubbles are shown in Fig. 1. Additional configurations with 6 and 18 bubbles can be found in Ref. [4]. As it is evident in Fig. 1, the dimensions of the bubbles in the experiments are small compared to that of the device, and the shapes of the inclusions are practically spherical.

Obviously, the observed ordering of the bubbles is due to a repulsive force induced by their interaction, but the nature of this force remains unclear so far. Our hypothesis is that the relative repulsion observed in the experiment is due to inertia effects on the scale of the bubbles. Byk *et al*. [4] computed the force acting on two circles in a simple shear flow of an inviscid liquid in 2D geometry and demonstrated that the interaction force is repulsive and decays relatively fast with the separation distance d as $1/d^5$, which agrees qualitatively with the observations. However, the experimental phenomenon takes place at moderate bubble Reynolds numbers (see Refs. [3,4]) and the flow in the experiments is far from being two dimensional. Thus, the applicability of the theoretical model of Ref. [4] is merely qualitative. The current work is devoted to another limiting case, e.g., small Reynolds number (Re). It follows from simple symmetry considerations that under the creeping flow conditions ($\mathrm{Re} = 0$) no interaction force is expected for two undeformed bubbles located at the same streamline in a simple shear flow. In this paper, we study the interaction of identical spherical bubbles in a simple shear for small but finite Reynolds numbers. A brief review of the results on the effect of finite inertia on the motion and interaction of solid and fluid particles in viscous flow is given below.

Series of works available in the literature concerns the motion of inclusions in linear low-Reynolds-number flows. Saffman [5,6] obtained the lift force on a small rigid sphere in a linear shear flow in the limit of small Reynolds number and large shear. His solution is based on a matched asymptotic expansion in which the flow in the inner region is modified by the inertia effects induced by the shear in the outer region. McLaughlin [7] extended Saffman's analysis by considering the case where inertia effects related to the mean flow are of the same order as those induced by the shear. Recently, Legendre and Magnaudet [8] reconsidered Saffman's and McLaughlin's analyses for a spherical drop of arbitrary viscosity. Their analytical solution is, therefore, valid for a spherical bubble with a vanishing viscosity. In that case the lift force was found to be $(2/3)^2$ times that of a solid sphere, the coefficient $2/3$ corresponds to the ratio of the magnitude of the vorticity at the surface of each kind of particle, which is also the ratio of translational resistance corresponding to a spherical bubble and a solid sphere in Stokes flow. McLaughlin [9] found that for the outer (inviscid) region the velocity in the direction of the shear-rate gradient (cross streamlines velocity) decays with the distance from the sphere in the same direction as $r^{-5/3}$. This result was used to evaluate the effect of a distant rigid wall on the lift force. Asmolov and Feuillebois [10]

[*]ceranjp@technunix.technion.ac.il
[†]ceolga@technunix.technion.ac.il
[‡]avinir@technunix.technion.ac.il

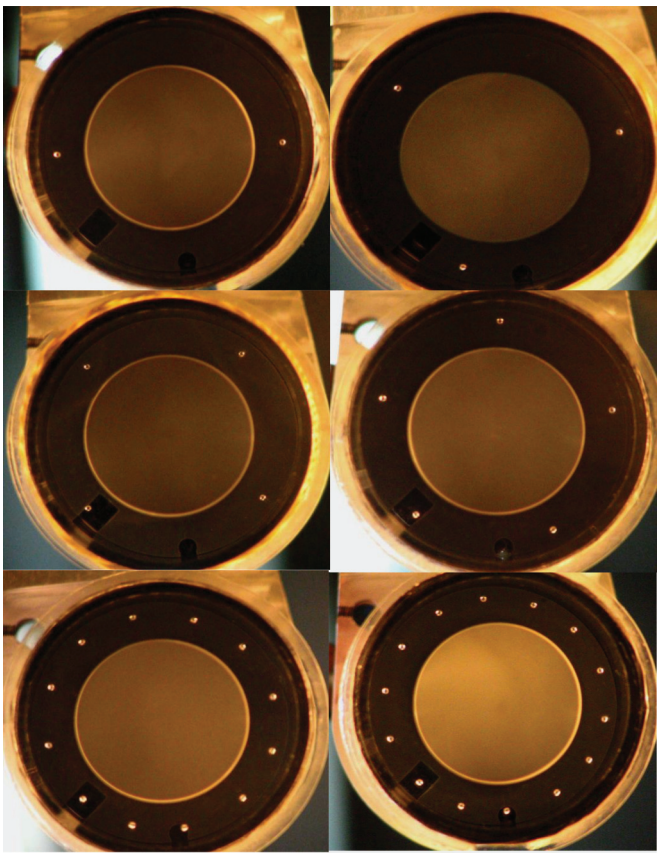

FIG. 1. (Color online) Top view of the bubble ring composed of 2, 3, 4, 5, 12, and 14 bubbles of the same size in a Couette device.

calculated the disturbance velocity induced by a solid particle in an unbounded shear flow, including the outer region and the viscous wakes. An essential feature of the above-mentioned papers is the role played by the velocity of the particle relative to the undisturbed fluid velocity at the position occupied by the particle. Indeed, the lift force is proportional to this relative velocity.

Another series of works concerns the effect of weak inertia on the flow field around neutrally buoyant inclusions in sheared flows. Lin *et al.* [11] employed the matched asymptotic expansion technique to study the case of a neutrally buoyant solid sphere immersed in an incompressible Newtonian fluid which, at large distances from the sphere, is in a state of simple shear flow. In particular, the inner expansion of the flow field was constructed in Ref. [11] up to $O(\mathrm{Re}^{3/2})$ terms and it was demonstrated that the effect of the outer region on the inner expansion enters first at this order, while $O(\mathrm{Re})$ terms are correctly predicted by the regular perturbation technique. Lin *et al.* [11] also studied the effect of the weak inertia on the suspension rheology in the infinitely dilute (noninteracting) limit. Ho and Leal [12] made use of a reciprocal theorem to study the $O(\mathrm{Re})$ inertia-induced lateral migration of a neutrally buoyant rigid sphere in a simple shear flow and two-dimensional Poiseuille flow, respectively, between solid walls. It is shown that the sphere reaches a stable lateral equilibrium position independent of the initial location of release, this position is midway between the walls for simple shear flow, and it is 0.3 of the channel width from the center line for Poiseuille flow. Subramanian *et al.* [13] extended the results of Ref. [11] to the case of viscous drops and dilute emulsions. Subramanian and Koch [14] showed that small fluid inertia alters the closed-streamline configuration in the near region of a neutrally buoyant sphere, predicted in the creeping flow limit. As a result, the streamlines are spiralling outward rather than closed.

Most of the analytic and semianalytic studies on inertial interaction of inclusions in viscous flow are devoted to interesting effects observed for sedimentation of small clusters of particles, such as unstable separating configurations, periodic or quasiperiodic trajectories, and chaotic solutions (see, e.g., Rosenstein and Leshansky [15] and the literature cited therein). Inertial effects on the pairwise interaction of inclusions were studied via numerical simulations at finite Re, making use of the lattice-Boltzmann (Kulkarni and Morris [16]), finite-element (Mikulencak and Morris [17]) and front tracking finite difference (Olapade *et al.* [18] and Singh and Sarkar [19]) methods. Kulkarni and Morris [16] obtained numerically reversing and spiralling trajectories of interacting solid particles pair in finite-inertia shear flow. Olapade *et al.* [18] simulated interaction of deformable drops, initially placed at the same shear plane, in the case of matched density and viscosity of the phases. It was found that the interacting drops show two distinct types of trajectory—drops passing each other similar to those seen in Stokes flow and drops reversing their trajectories on coming together. Singh and Sarkar [19] extended the investigations of Ref. [18] to cases where the viscosity of the dispersed phase differs from that of the matrix, and drops are initially placed in different shear planes.

In this paper, we report on the analytical study of the leading-order effect of weak inertia on the interaction of identical spherical bubbles freely suspended in a simple shear flow. We also suggest three simplified models of interaction of bubbles in a Couette-Taylor device that are based on the results of this analytical study and compare the results of the bubbles dynamic simulations to the experimental measurements. The paper is organized as follows: In Sec. II, the problem of the interaction of two spherical bubbles in a simple shear flow is formulated and expansion of solutions in powers of Re is discussed, and two methods are employed to construct the zeroth-order solutions. In Sec. II C the reciprocal theorem is used to obtain the leading-order term of the inertia-induced force on the interacting bubbles in the form of a volume integral depending solely on the solution of the creeping flow equations, and the computed force is presented as function of the separation distance. In Sec. III, we formulate three simplified models of the dynamics of bubbles in a Couette-Taylor vortex. Further, we present the experimental observations on such a dynamic interaction and compare them to the dynamic simulations according to the theoretical models. Conclusions and discussion are given in Sec. IV.

II. TWO BUBBLES IN A SIMPLE SHEAR FLOW

A. Formulation of the problem

Consider two stationary spherical bubbles of equal radii a suspended in an incompressible fluid of viscosity μ and density ρ, which is subjected to an unbounded simple shear

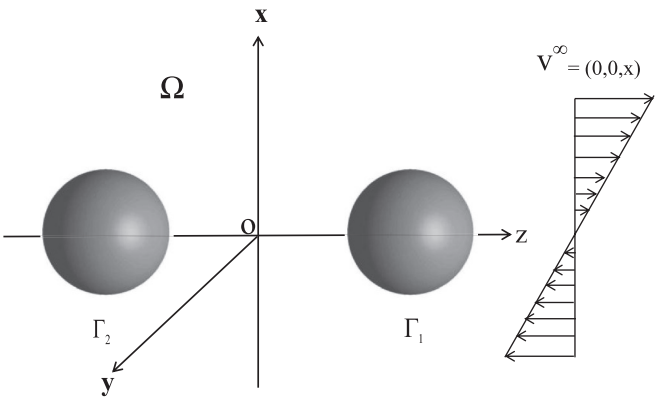

FIG. 2. Geometry of the problem.

flow field $\mathbf{v}^* = (0,0,Gx^*)$ along the z axis, where G is the shear rate. The location of the bubbles is assumed to be on the same streamline $x = y = 0$.

In the following analysis, length, velocity, and stress will be nondimensionalized using a, Ga, and μG, respectively. Let Ω be the domain occupied by the continuous fluid, Γ_i, $i = 1,2$ denote the boundary of the bubbles, and d be the distance between the centers of the bubbles (see Fig. 2).

Let $\mathbf{v}$, p, and $\boldsymbol{\sigma}$ denote the scaled disturbances of velocity, dynamic pressure, and stress fields, respectively, due to the presence of the bubbles. The disturbed flow around the bubbles is governed by the steady Navier-Stokes equations,

$$\begin{aligned}\nabla^2\mathbf{v} - \nabla p &= \nabla\cdot\boldsymbol{\sigma}\\ &= \mathrm{Re}[(\mathbf{v}\cdot\nabla)\mathbf{v} + (\mathbf{v}^\infty\cdot\nabla)\mathbf{v} + (\mathbf{v}\cdot\nabla)\mathbf{v}^\infty], \qquad (1)\end{aligned}$$

$$\nabla\cdot\mathbf{v} = 0, \quad \mathbf{x}\in\Omega, \qquad (2)$$

where $\mathrm{Re} = \rho G a^2/\mu$ is the Reynolds number and $\mathbf{v}^\infty = (0,0,x)$. At the boundaries of the bubbles, Γ_1 and Γ_2, and far from the inclusions the stress and the velocity satisfy

$$(\boldsymbol{\sigma} + \boldsymbol{\sigma}^\infty)\cdot\mathbf{n} = \frac{\nabla\cdot\mathbf{n}}{\mathrm{Ca}}\mathbf{n}, \quad \mathbf{x}\in\Gamma_i, \quad i = 1,2, \qquad (3)$$

$$\mathbf{v}\cdot\mathbf{n} = -\mathbf{v}^\infty\cdot\mathbf{n}, \quad \mathbf{x}\in\Gamma_i, \quad i = 1,2, \qquad (4)$$

$$\mathbf{v}\to\mathbf{0} \quad \text{as} \quad |\mathbf{x}|\to\infty. \qquad (5)$$

Here $\mathbf{n}$ is the unit normal vector pointing into the fluid, $\boldsymbol{\sigma}^\infty$ is the stress tensor corresponding to the basic flow $\mathbf{v}^\infty$, and $\mathrm{Ca} = \mu a G/\gamma$ is the capillary number, with γ being the constant surface tension.

In order to isolate the effect of inertia on the interaction of the bubbles and in agreement with the high surface tension at the fluid-air interface and small dimensions of the bubbles in the experiments of Refs. [3] and [4] we assume absence of gravity and Ca vanishingly small. Under this assumption, the bubbles remain spherical and condition (3) reduces to

$$\boldsymbol{\sigma}:\mathbf{ns} = -\boldsymbol{\sigma}^\infty:\mathbf{ns}, \quad \mathbf{x}\in\Gamma_i, \quad i = 1,2, \qquad (6)$$

where the colons denote scalar product between tensors and $\mathbf{s}$ is an arbitrary tangential vector to the bubble surface. In this paper, we are interested in the interaction of bubbles located along the same streamline in the shear flow, $x = y = 0$ (see Fig. 2).

Further, we assume a small but finite Reynolds number and look for a solution in the form of an expansion in terms of Re. At $\mathrm{Re} = 0$, Eqs. (1) and (2) become the steady Stokes equations,

$$\nabla\cdot\boldsymbol{\sigma} = \mathbf{0}, \quad \nabla\cdot\mathbf{v} = 0, \quad \mathbf{x}\in\Omega. \qquad (7)$$

Let $\mathbf{v}^0, \boldsymbol{\sigma}^0$ be a solution of (4)–(7). It seems natural to consider $\mathbf{v}^0$, $\boldsymbol{\sigma}^0$ as a leading-order approximation of the solution of (1), (2), and (4)–(6). However, as in the case of a single inclusion in a simple shear, it is not a uniformly valid approximation in an unbounded domain at any finite Re, whatever small. For a single drop, this approximation breaks down for distances from the inclusions of $O(\mathrm{Re}^{-1/2})$ and the correct approximation to the velocity field in this outer region must be obtained from a solution of the linearized Navier-Stokes equations (1). The two cases, $d < O(\mathrm{Re}^{-1/2})$ and $d > O(\mathrm{Re}^{-1/2})$, with d being the separation distance between two bubbles submerged in the fluid, should be considered separately and, in this paper, we concentrate on the first case when the two inclusions have a common inner region. The second case is briefly discussed at the end of Sec. II C.

Previous studies [11,13] employed a matched asymptotic expansions technique to evaluate the velocity field around a rigid sphere and a single drop in a linear flow and obtained the inner expansion up to $O(\mathrm{Re}^{3/2})$. Also, it was demonstrated that the formal use of regular perturbations provides a correct result for the leading-order $O(\mathrm{Re})$ perturbations in the vicinity of the inclusions. These results can be directly applied to a multibubble case, when the inclusions are located in a common inner region, yielding that, in the inner region, the expansions can be expressed as

$$\begin{aligned}\mathbf{v} &= \mathbf{v}^0 + \mathrm{Re}\mathbf{v}^1 + O(\mathrm{Re}^{3/2}),\\ p &= p^0 + \mathrm{Re}p^1 + O(\mathrm{Re}^{3/2}),\\ \boldsymbol{\sigma} &= \boldsymbol{\sigma}^0 + \mathrm{Re}\boldsymbol{\sigma}^1 + O(\mathrm{Re}^{3/2}).\end{aligned} \qquad (8)$$

The individual terms $(\mathbf{v}^0, p^0, \boldsymbol{\sigma}^0)$ and $(\mathbf{v}^1, p^1, \boldsymbol{\sigma}^1)$ satisfy the equations

$$\begin{aligned}\nabla^2\mathbf{v}^0 - \nabla p^0 &= \nabla\cdot\boldsymbol{\sigma}^0 = \mathbf{0},\\ \nabla\cdot\mathbf{v}^0 &= 0, \quad \mathbf{x}\in\Omega,\\ \mathbf{v}^0\cdot\mathbf{n} &= -\mathbf{v}^\infty\cdot\mathbf{n}, \quad \boldsymbol{\sigma}^0:\mathbf{ns} = -\boldsymbol{\sigma}^\infty:\mathbf{ns},\\ \mathbf{x} &\in \Gamma_i, \quad i = 1,2,\\ \mathbf{v}^0 &\to \mathbf{0} \quad \text{as} \quad |\mathbf{x}|\to\infty.\end{aligned} \qquad (9)$$

and

$$\begin{aligned}\nabla^2\mathbf{v}^1 - \nabla p^1 &= \nabla\cdot\boldsymbol{\sigma}^1\\ &= (\mathbf{v}^0\cdot\nabla)\mathbf{v}^0 + (\mathbf{v}^\infty\cdot\nabla)\mathbf{v}^0 + (\mathbf{v}^0\cdot\nabla)\mathbf{v}^\infty,\\ \nabla\cdot\mathbf{v}^1 &= 0, \quad \mathbf{x}\in\Omega,\\ \mathbf{v}^1\cdot\mathbf{n} &= 0, \quad \boldsymbol{\sigma}^1:\mathbf{ns} = 0, \quad \mathbf{x}\in\Gamma_i, \quad i = 1,2.\end{aligned} \qquad (10)$$

B. Solution of the zeroth order

In order to solve the zeroth-order problem (9), i.e., creeping flow field, we adopt two different methods, namely bispherical coordinates and method of reflections. Below, we give the solution methodology in brief.

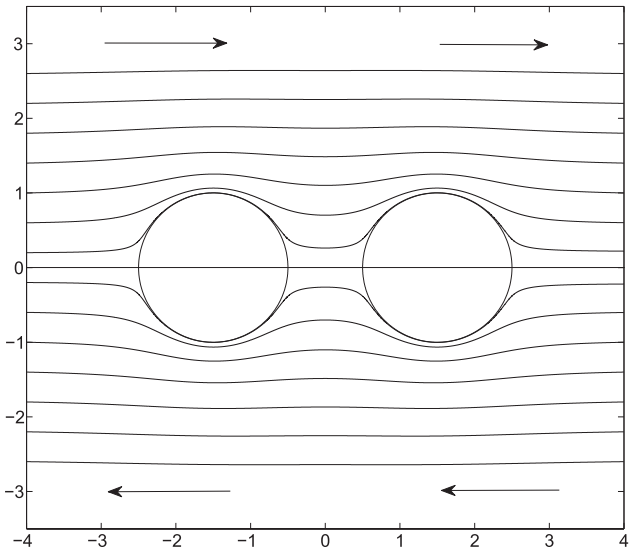

FIG. 3. Flow pattern around two bubbles in a creeping simple shear flow at the midplane $y = 0$ and separation distance $d = 3$.

Following Lin, Lee, and Sather [20], the general solution of the Stokes equation in the bispherical coordinates is presented in the form of a series in spherical harmonics, and coefficients of the series are determined from the boundary conditions. The details of this procedure are presented in the Appendix. The advantage of bispherical coordinate systems is that it allows one to satisfy boundary conditions on two bubbles simultaneously. The cross-section plot of the flow around two equal-size bubbles with separation distance $d = 3$ is shown in Fig. 3.

Note that closed streamlines regions, surrounding either of the bubbles or both, were not found for close proximity or large separation. This is in contrast to observations in the cases of solid particles [21,22] and of viscous drops [23], where both open and closed streamlines exist in a Couette flow. The solution also yields that, at any value of d, the flow does not separate at the bubble surfaces, reflecting the zero tangential stress there. Furthermore, as can be observed in Fig. 3, the velocity disturbance in the lateral direction decays rather fast. It follows from simple symmetry considerations that in the creeping simple shear flow, no force is exerted on spherical bubbles located at the zero streamline. This result can also be obtained by a direct calculation. Hence, it follows that the velocity disturbance decays as $1/|\mathbf{x}|^2$ at infinity.

We present the solution of the two-bubble problem in shear flow using an approximate method called method of reflections for calculating the force exerted on the two bodies. This method complements the solution via bispherical coordinates since it can be easily extended to study multiparticle systems. For the two spherical bubbles in Fig. 4, the solution is presented in the form

$$\mathbf{v}^0 = \sum_{i=1}^{2}\sum_{k=1}^{\infty}\mathbf{v}^0_{i,k}(r_i,\theta_i,\phi), \quad \boldsymbol{\sigma}^0 = \sum_{i=1}^{2}\sum_{k=1}^{\infty}\boldsymbol{\sigma}^0_{i,k}(r_i,\theta_i,\phi),$$
$$p^0 = \sum_{i=1}^{2}\sum_{k=1}^{\infty}p^0_{i,k}(r_i,\theta_i,\phi), \tag{11}$$

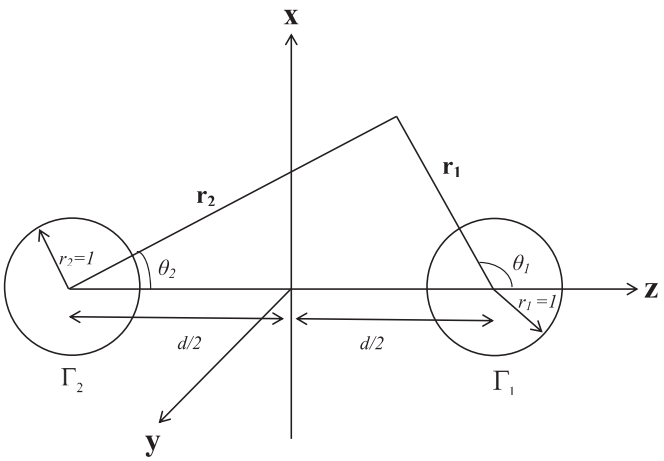

FIG. 4. Spherical coordinate systems connected to two bubbles.

where (r_i,θ_i,ϕ) are spherical coordinate systems originating at the center of bubble i. Here $\mathbf{v}^0_{i,k}$ is the solution of the Stokes equations in the domain $r_i > 1$, decaying at infinity, with the index k indicating the number of reflections and with $\mathbf{v}^0_{i,0}$ satisfying the conditions (4) and (6) at $r_i = 1$, while

$$\mathbf{v}^0_{i,k+1}\cdot\mathbf{n} = -\mathbf{v}^0_{j,k}\cdot\mathbf{n},$$
$$\boldsymbol{\sigma}^0_{i,k+1}:\mathbf{ns} = -\boldsymbol{\sigma}^0_{j,k}:\mathbf{ns}, \quad \mathbf{x}\in\Gamma_i, \quad i\neq j. \tag{12}$$

It is easy to show that

$$\mathbf{v}^0 = -\frac{1}{r_1^2}\sin\theta_1\cos\theta_1\cos\phi\,\mathbf{e}_{r_1} - \frac{1}{r_2^2}\sin\theta_2\cos\theta_2\cos\phi\,\mathbf{e}_{r_2} + O\left(\frac{1}{d^3}\right), \tag{13}$$

where $\mathbf{e}_{r_1},\mathbf{e}_{r_2}$ are unit vectors with respect to spherical coordinate systems in the direction of increasing r_1,r_2, respectively. From (13) it may be concluded that the velocity field decays as $O(1/|\mathbf{x}|^2)$ at infinity, which is consistent with the argument presented above (zero net force). Note that the generalization of this method to a multiparticle case is straightforward.

C. Force exerted on bubbles at small Re

As mentioned above, the zeroth-order solution provides no net force on the bubbles. Since the force exerted on each inclusion by the flow is obviously determined by the stress field in the vicinity of it, i.e., by the inner expansion, one can conclude that this force is of $O(\mathrm{Re})$,

$$F_i = \mathrm{Re}\oint_{\Gamma_i}\boldsymbol{\sigma}^1\cdot\mathbf{n}d\Gamma + O(\mathrm{Re}^{3/2}), \quad i = 1,2, \tag{14}$$

where $\boldsymbol{\sigma}^1$ results from the $O(\mathrm{Re})$ problem; see (10). Ho and Leal [12], who addressed the Segre Silberberg effect of lateral migration of solid spherical particles embedded in shear flow due to inertia effects at small Reynolds numbers, suggested that it was not necessary to obtain a detailed solution of (10) to calculate (14). Instead of constructing $\mathbf{v}^1$ and $\boldsymbol{\sigma}^1$ explicitly, they proposed to employ the well-known Lorentz reciprocal theorem to obtain the leading-order term for the expansion of the force in the form of a volume integral depending solely

on $\mathbf{v}^0$ and $\boldsymbol{\sigma}^0$. This approach is followed here to calculate the force on the bubbles induced by the small inertia effect.

We define an auxiliary problem. Let $\mathbf{u}$ and $\boldsymbol{\tau}$ be a solution of

$$\begin{aligned} \nabla^2\mathbf{u} - \nabla q &= \nabla\cdot\boldsymbol{\tau} = \mathbf{0}, \quad \nabla\cdot\mathbf{u} = 0, \quad \mathbf{x}\in\Omega, \\ \mathbf{u} &\to \mathbf{0} \quad \text{as} \quad |\mathbf{x}|\to\infty, \\ \mathbf{u}\cdot\mathbf{n} &= \mathbf{e}_z, \quad \boldsymbol{\tau}:\mathbf{ns} = 0, \quad \mathbf{x}\in\Gamma_1, \\ \mathbf{u}\cdot\mathbf{n} &= -\mathbf{e}_z, \quad \boldsymbol{\tau}:\mathbf{ns} = 0, \quad \mathbf{x}\in\Gamma_2, \end{aligned} \tag{15}$$

with $\mathbf{e}_z$ being a unit vector along the z axis, i.e., the anticipated departure direction of the bubbles. Application of the reciprocal theorem (see, e.g., Ho and Leal [12], Subramanian and Koch [14], and Kim and Karrila [24]) to the fields $\mathbf{v}^1,\boldsymbol{\sigma}^1$ and $\mathbf{u},\boldsymbol{\tau}$ results in

$$\oint_{\Gamma_1\cup\Gamma_2}\mathbf{n}\cdot\boldsymbol{\sigma}^1\cdot\mathbf{u}d\Gamma - \oint_{\Gamma_1\cup\Gamma_2}\mathbf{n}\cdot\boldsymbol{\tau}\cdot\mathbf{v}^1 d\Gamma = \int_\Omega \mathbf{f}\cdot\mathbf{u}d\Omega, \tag{16}$$

where $\mathbf{f}$ is the inhomogeneous part of the governing equation (10), i.e.,

$$\mathbf{f} = (\mathbf{v}^0\cdot\nabla)\mathbf{v}^0 + (\mathbf{v}^\infty\cdot\nabla)\mathbf{v}^0 + (\mathbf{v}^0\cdot\nabla)\mathbf{v}^\infty. \tag{17}$$

The identity (16) has been written assuming that the corresponding surface integrals vanish at infinity and the volume integral in its right-hand side is absolutely convergent. This is, indeed, the case since the auxiliary velocity field $\mathbf{u}$ decays as $O(1/|\mathbf{x}|^2)$ for large $|\mathbf{x}|$, because the bubbles are translating in opposite directions and the $O(1/|\mathbf{x}|)$ terms cancel each other at large distances, and the corresponding stress fields decays as $O(1/|\mathbf{x}|^3)$, while the disturbance velocity $\mathbf{v}^1$ is bounded at infinity and the disturbance stress decays as $O(1/|\mathbf{x}|)$.

The second term in the left-hand side of (16) vanishes due to the boundary conditions of zero tangential stress for the auxiliary fields and zero normal disturbance velocity. The first term in the left-hand side of (16) becomes

$$\begin{aligned} \oint_{\Gamma_1\cup\Gamma_2}\mathbf{n}\cdot\boldsymbol{\sigma}^1\cdot\mathbf{u}d\Gamma &= \oint_{\Gamma_1}\mathbf{n}\cdot\boldsymbol{\sigma}^1\cdot\mathbf{u}d\Gamma + \oint_{\Gamma_2}\mathbf{n}\cdot\boldsymbol{\sigma}^1\cdot\mathbf{u}d\Gamma \\ &= \oint_{\Gamma_1}\mathbf{n}\cdot\boldsymbol{\sigma}^1\cdot\mathbf{e}_z d\Gamma - \oint_{\Gamma_2}\mathbf{n}\cdot\boldsymbol{\sigma}^1\cdot\mathbf{e}_z d\Gamma, \end{aligned} \tag{18}$$

i.e., it equals the sum of the force exerted by the flow $\mathbf{v}^1,\boldsymbol{\sigma}^1$ on bubble 1 in the direction of axis z, F^1, and the force exerted on bubble 2 in the opposite direction. Due to the symmetry of the problem, these two forces are equal. Hence,

$$F^1 = \frac{1}{2}\int_\Omega \mathbf{f}\cdot\mathbf{u}d\Omega, \tag{19}$$

and the force exerted on bubble 1 in the direction of axis z, at the leading order, is

$$F = \mathrm{Re}F^1 = \frac{\mathrm{Re}}{2}\int_\Omega \mathbf{f}\cdot\mathbf{u}d\Omega. \tag{20}$$

The calculation of the force on a bubble requires solution of two problems for the creeping flow: the one for the zeroth-order expansion term $\mathbf{v}^0,\boldsymbol{\sigma}^0$ and the other for the auxiliary problem (15), $\mathbf{u}$ and $\boldsymbol{\tau}$. In order to solve the latter, we adopt the two methods, namely the bispherical coordinates system and method of reflections, as described before. For the axisymmetric auxiliary solution, application of the bispherical coordinate system follows the classical approach for axisymmetric problems (see, e.g., Stimson and Jeffrey [25]) and is not detailed here. The integral in (20) is, consequently, evaluated numerically for any separation distance, d, to satisfy the desired accuracy. Application of the method of reflections to (15) provides the explicit expression for the velocity

$$\begin{aligned} \mathbf{u} = \Bigg[&\left(1+\frac{1}{d}+\frac{1}{d^2}\right)\left(\frac{1}{r_1}\cos\theta_1\mathbf{e}_{r_1} - \frac{1}{r_2}\cos\theta_2\mathbf{e}_{r_2}\right. \\ &\left. - \frac{1}{2r_1}\sin\theta_1\mathbf{e}_{\theta_1} + \frac{1}{2r_2}\sin\theta_2\mathbf{e}_{\theta_2}\right) + \frac{1}{2d^2}\frac{1}{r_1^2}(3\cos^2\theta_1 - 1)\mathbf{e}_{r_1} \\ &+ \frac{1}{2d^2}\frac{1}{r_2^2}(3\cos^2\theta_2 - 1)\mathbf{e}_{r_2} + O\left(\frac{1}{d^3}\right)\Bigg]. \end{aligned} \tag{21}$$

Thus, substituting (17) and (21) into (19) and performing analytical integration results in

$$F^1 = \frac{2\pi}{9}\left(1+\frac{1}{d}-\frac{4}{5}\frac{1}{d^2}\right) + O\left(\frac{1}{d^3}\right). \tag{22}$$

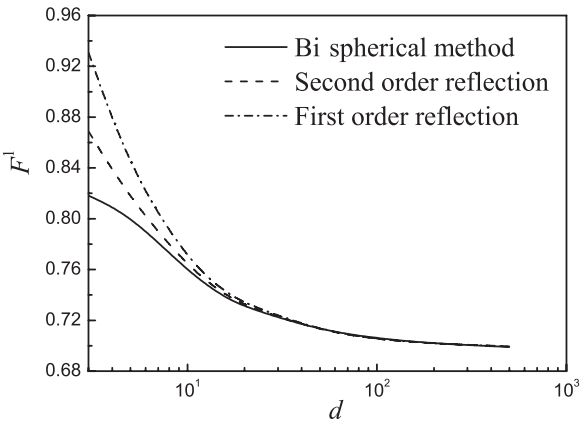

FIG. 5. Force exerted on the right bubble in a pair of bubbles embedded in a simple shear flow. The solid curve is calculated by making use of bispherical coordinates. Dashed and dashed-dotted curves are calculated by use of the reflection method with the accuracies $O(1/d^2)$ and $O(1/d)$, respectively.

The forces calculated by the two methods are depicted and compared in Fig. 5 where logarithmic scale is used for d. Solid curve is calculated making use of bispherical coordinates. Dashed and dashed-dotted curves are calculated by the reflection method with the accuracy $O(1/d^2)$ and $O(1/d)$, respectively. It may be noted that at relatively large separation distance, both methods estimate the force in excellent agreement. Thus, for $d > 5$, the difference between the "exact solution" computed via bispherical coordinates and approximate ones calculated by the reflection method, with the accuracy $O(1/d)$ and $O(1/d^2)$, does not exceed 10% and 5%, respectively. For $d > 20$, the results of both variants of reflection method are within 0.5% of the exact solution.

An immediate conclusion from the calculations presented in Fig. 5 is that the force is of a repulsive nature and that it decreases with the growth of the separation distance between bubbles and, as this distance tends to infinity, it approaches a nonzero limiting value, $F^1 \to 2\pi/9 \approx 0.6981$. Note, though,

that these results are obtained under the assumption that the bubbles share a common inner region, i.e., that the distance between them does not exceed $O(\mathrm{Re}^{-1/2})$. Also, F^1 is multiplied by the expansion parameter Re [see Eq. (20)]. The larger the distance between the bubbles the smaller is Re for which the two bubbles remain located in the mutual viscous region. Note also that the situation that occurs when this effect of weak inertia on the interaction of inclusions that share a common inner (outer) region in a fluid does not vanish at large separation is typical also for the interaction of particles settling under gravity (see, e.g., Rosenstein and Leshansky [15] and the literature cited therein for further examples). The contribution of the outer region should be added to the above analysis in order to render the calculation of the force complete. When the separation, $d \geqslant O(\mathrm{Re}^{-1/2})$, a noninteracting model developed in, e.g., Subramanian *et al.* [13] can be applied. Nevertheless, as is discussed below, it is possible that the above analysis of this section is sufficient for the study of the dynamics of bubble interaction located on the center streamline in the core of a vortex of the Couette device, where typical separations between the bubbles are moderate and consideration of the case $d \geqslant O(\mathrm{Re}^{-1/2})$ is not required.

III. BUBBLE DYNAMICS IN A COUETTE DEVICE

A. Simplified models

In order to apply the results of Sec. II C to the motion of bubbles in a Couette-Taylor device, we formulate here simplified models of the process. Consider N spherical bubbles of unit radii located along a center closed streamline in a Taylor vortex. Let l be the length of this streamline and l_n be the distance between bubbles n and $n+1$. Note that if N bubbles of unit radii are present it follows that l must be larger than $2N$. The distance between bubbles 1 and N can be written as

$$l_N = l - \sum_{n=1}^{N-1} l_n \quad (N \geqslant 2). \tag{23}$$

The values l_n change dynamically due to the repulsive force experienced by bubbles embedded in the shear flow and the drag felt by the bubbles during their relative motion. The following assumptions are made in order to simplify the model

(i) Interaction is mostly due to the primary shear flow that is considered unbounded in all directions. The effect of the Taylor vortex in the experiment that keeps bubbles at certain horizontal position in the experiment corresponds to the absence of gravity in the model.

(ii) The primary flow is modeled by a unidirectional simple shear, neglecting nonzero curvature of the streamlines. This follows from the diminishingly small ratio of bubble to streamline radii.

(iii) The velocity of translation of bubbles along the streamline connecting their centers results from a balance between the repulsive force induced by the inertia in the shear flow and the viscous resistance to this translation.

We consider three models of the process that differ in the assumed mode of bubble interaction: (i) the nearest-neighbors interaction model, (ii) the pairwise interaction model, and (iii) the periodic model.

Model (i) assumes that each bubble interacts solely with its nearest neighbors. Thus, following (22), it can be calculated to $O(1/d^2)$. Model (ii) assumes the pairwise interaction, i.e., that each bubble interacts with every other bubble in the ring as if the others are not present, with the resulting force on each bubble being the sum of all forces resulting from these pairwise interactions. This assumption is valid for relatively large separations between the bubbles and with the accuracy of $O(1/d)$, with d denoting the minimal separation. Model (iii) extends the number of pairwise interactions in model (ii) by considering an infinite periodic structure. Thus, models (ii) and (iii) assume that the repulsive force exerted on a bubble in a simple shear flow due to the presence of another bubble somewhere in the field separated by distance δ, contributes to the total force,

$$F = \mathrm{Re} F_1^1(\delta), \quad F_1^1(\delta) = \frac{2\pi}{9}\left(1 + \frac{1}{\delta}\right) + O\left(\frac{1}{\delta^2}\right). \tag{24}$$

According to the assumptions of model (i), the force exerted on the n^{th} bubble by the shear flow equals $\mathrm{Re}[F^1(l_{n-1}) - F^1(l_n)]$, where F^1 is defined in (22) and which is balanced by the Stokes drag on this bubble calculated by taking into account the presence of translating $(n-1)^{\text{th}}$ and $(n+1)^{\text{th}}$ bubbles. Hence, the force balance on the bubbles has the form

$$\begin{aligned}
&R_{1,N}U_N + R_{1,1}U_1 + R_{1,2}U_2 = \mathrm{Re}[F^1(l_N) - F^1(l_1)],\\
&R_{n,n-1}U_{n-1} + R_{n,n}U_n + R_{n,n+1}U_{n+1}\\
&\quad = \mathrm{Re}[F^1(l_{n-1}) - F^1(l_n)], \quad n = 2,\ldots,N-1,\\
&R_{N,N-1}U_{N-1} + R_{N,N}U_N + R_{N,N+1}U_{N+1}\\
&\quad = \mathrm{Re}[F^1(l_{N-1}) - F^1(l_N)],
\end{aligned} \tag{25}$$

where $R_{n,m}(n = 1,\ldots,N; m = n-1,n,n+1)$ is the viscous force exerted on the n^{th} bubble by the Stokes flow induced by the translational motion of the m^{th} bubble with unit velocity in the otherwise quiescent fluid in a three bubble ($n-1$,n and $n+1$) configuration, and U_n is the velocity of bubble n. Note that the large separation limit of F^1 discussed in Sec. II C is canceled on the right-hand side of (25) and, thus, has no effect on the dynamics of bubbles.

Assume now that all the separations are larger than the bubble diameters and are of the same order of magnitude ($l_n = O(d), d \gg 1, n = 1,\ldots,N$). It follows from (22) that the right-hand side of (25) contains the terms of $O(1/d)$ and of $O(1/d^2)$ since the $O(1)$ terms cancel. In order to obtain U_n with the accuracy of $O(1/d^2)$, it is sufficient to have $R_{n,m}$ with the accuracy of $O(1/d)$. The use of the reflection method results in (see also Happel and Brenner [26])

$$\begin{aligned}
&R_{n,n} = -4\pi + O\left(\frac{1}{d^2}\right), \quad R_{n,n-1} = \frac{4\pi}{l_{n-1}} + O\left(\frac{1}{d^2}\right),\\
&R_{n,n+1} = \frac{4\pi}{l_n} + O\left(\frac{1}{d^2}\right), \quad n = 2,\ldots,N-1,\\
&R_{N,1} = R_{1,N} = \frac{4\pi}{l_N} + O\left(\frac{1}{d^2}\right),\\
&R_{1,1} = R_{N,N} = -4\pi + O\left(\frac{1}{d^2}\right).
\end{aligned} \tag{26}$$

According to models (ii) and (iii), the force balance on the n^{th} bubble reads, respectively,

$$4\pi U_n = \mathrm{Re}\left\{\sum_{k=n}^{N-1}\left[F_1^1\left(\sum_{j=0}^{k-1} l_{n+j}\right) - F_1^1\left(l-\sum_{j=0}^{k-1} l_{n+j}\right)\right] + \sum_{k=1}^{n-1}\left[F_1^1\left(l-\sum_{j=1}^{k} l_j\right) - F_1^1\left(\sum_{j=1}^{k} l_j\right)\right]\right\}$$

$$= \mathrm{Re}\frac{2\pi}{9}\left[\sum_{k=n}^{N-1}\left(\frac{1}{\sum_{j=0}^{k-1} l_{n+j}} - \frac{1}{l-\sum_{j=0}^{k-1} l_{n+j}}\right) + \sum_{k=1}^{n-1}\left(\frac{1}{l-\sum_{j=1}^{k} l_j} - \frac{1}{\sum_{j=1}^{k} l_j}\right)\right], \quad n = 1,\ldots,N, \tag{27}$$

and

$$4\pi U_n = \mathrm{Re}\sum_{m=1}^{\infty}\left(\sum_{k=n}^{N-1}\left\{F_1^1\left[(m-1)l - \sum_{j=0}^{k-1} l_{n+j}\right] - F_1^1\left(ml - \sum_{j=0}^{k-1} l_{n+j}\right)\right]\right.$$

$$\left. + \sum_{k=1}^{n-1}\left[F_1^1\left(ml - \sum_{j=1}^{k} l_j\right) - F_1^1\left((m-1)l - \sum_{j=1}^{k} l_j\right)\right\}\right)$$

$$= \mathrm{Re}\frac{2\pi^2}{9l}\left[\sum_{k=n}^{N-1}\cot\left(\pi\sum_{j=0}^{k-1}\frac{l_{n+j}}{l}\right) - \sum_{k=1}^{n-1}\cot\left(\pi\sum_{j=1}^{k}\frac{l_j}{l}\right)\right], \quad n = 1,\ldots,N. \tag{28}$$

Note that the consideration of a periodic structure results in a considerable simplification of the expression (27).

The system of Eqs. (25), (27), and (28) can be solved with respect to U_n, resulting in

$$U_n = \mathrm{Re}G_n^{(k)}(l_1,\ldots,l_N), \quad n = 1,\ldots,N, \quad k = i,ii,iii, \tag{29}$$

and the temporal evolution of l_n is governed by

$$\frac{dl_n}{dT} = \mathrm{Re}\Phi_n^{(k)}(l_1,\ldots,l_N), \quad \text{where} \quad \Phi_n^{(k)}(l_1,\ldots,l_N)$$
$$= G_{n+1}^{(k)}(l_1,\ldots,l_N) - G_n^{(k)}(l_1,\ldots,l_N), \tag{30}$$

and with T denoting the time. Obviously $\sum_{n=1}^{N}\Phi_n^{(k)} = 0$, and, hence, $\sum_{n=1}^{N} l_n$ is an integral of (30) that we use to reduce the order of the system. For example, we consider the first $(N-1)$ equations in (30) after substituting l_N from (23). Finally, we stretch the time by the Reynolds number, $t = \mathrm{Re}T$ and obtain the following dynamic system:

$$\frac{dl_n}{dt} = \Phi_n^{(k)}\left(l_1,\ldots,l_{N-1},l-\sum_{n=1}^{N-1} l_n\right),$$
$$n = 1,2,\ldots,N-1, \quad k = i,ii,iii, \tag{31}$$

In the case of two bubbles system for model (i) that corresponds to the nearest-neighbor interaction model, (31) reduces to a single first-order ordinary differential equation,

$$\frac{dl_1}{dt} = \Phi_1^{(i)}(l_1,l-l_1)$$
$$= \frac{1}{9}\left[\frac{1}{l_1} - \frac{1}{l-l_1} - \frac{9}{5l_1^2} + \frac{9}{5(l-l_1)^2}\right], \tag{32}$$

where all the terms of the order $\geqslant O(1/d^3)$ in the right-hand side are neglected. The pairwise interaction model (ii) results in the equation

$$\frac{dl_1}{dt} = \Phi_1^{(ii)}(l_1,l-l_1) = \frac{1}{9}\left(\frac{1}{l_1} - \frac{1}{l-l_1}\right), \tag{33}$$

whereas the periodic model (iii) leads to

$$\frac{dl_1}{dt} = \Phi_1^{(iii)}(l_1,l-l_1) = \frac{\pi}{9l}\cot\left(\frac{\pi l_1}{l}\right). \tag{34}$$

Recall that the models are applied to the motion of two bubbles of unit radii along the streamline of length l that requires $l \gg 4$. Under this condition, it follows from each of equations (32), (33), or (34) that

$$\Phi_1^{(k)}(l_1,l-l_1) > 0 \text{ if } l_1 < l/2 \quad \text{and}$$
$$\Phi_1^{(k)}(l_1,l-l_1) < 0 \text{ if } l_1 > l/2.$$

Hence, the smaller separation grows monotonically and the larger one decreases monotonically with time. Also, all these equations can be solved analytically. Thus solution of (32) and (33) can be expressed as

$$t = \int_{l_1(0)}^{l_1}\frac{d\zeta}{\Phi_1^i(\zeta,l-\zeta)} = \frac{9}{4}\left[l_1^2 - ll_1 - l_1^2(0) + ll_1(0)\right]$$
$$+ \frac{729l}{25l-80}\ln\left|\frac{9l-5ll_1+5l_1^2}{9l-5ll_1(0)+5l_1^2(0)}\right|$$
$$- \frac{45l^3}{8(5l-36)}\ln\left|\frac{2l_1-l}{2l_1(0)-l}\right| \tag{35}$$

and

$$t = \frac{9}{4}\left[l_1^2 - ll_1 - l_1(0)^2 + ll_1(0)\right] - \frac{9l^2}{8}\ln\left|\frac{2l_1-l}{2l_1(0)-l}\right|, \tag{36}$$

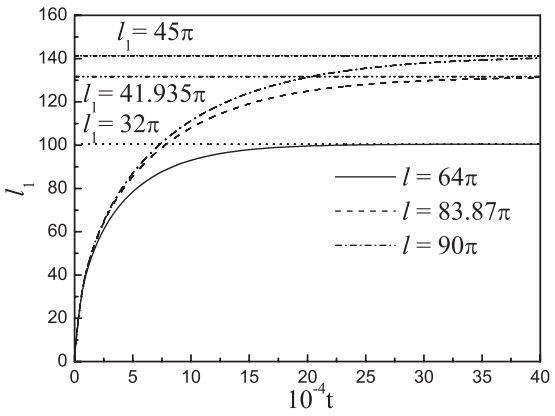

FIG. 6. Evolution of the minimum separation distance between two bubbles for various lengths of the center streamline in the Couette device, calculated following model (i) [Eq. (35)].

respectively. Analytical solution of (34) is

$$l_1(t) = \frac{l}{\pi}\arccos\left[\cos\left(\frac{\pi}{l}l_1(0)\right)\exp\left(-\frac{\pi^2}{9l^2}t\right)\right]. \quad (37)$$

Obviously, for all three models, $l_1 \to l/2$ as $t \to \infty$.

Note that Eqs. (32), (33), and (34) depend on a single parameter l. Figure 6 shows the evolution of separation distance between two bubbles for various streamline lengths (l), i.e., $l = 64\pi, 83.87\pi, 90\pi$ (the length 83.87π corresponds to the experiments presented in the next subsection) computed via nearest-neighbors interaction model (i).

It may be observed that, as expected, the relaxation time increases with the length of streamline.

Equations (33) and (34) allow a transformation of variables in the form

$$\zeta_1 = \frac{l_1}{l}, \quad t_1 = \frac{t}{l^2}, \quad (38)$$

which eliminates the parameter l. Hence,

$$\frac{d\zeta_1}{dt_1} = \Phi_1^{(ii)}(\zeta_1, 1-\zeta_1) = \frac{1}{9}\left(\frac{1}{\zeta_1} - \frac{1}{1-\zeta_1}\right) \quad (39)$$

and

$$\frac{d\zeta_1}{dt_1} = \Phi_1^{(iii)}(\zeta_1, 1-\zeta_1) = \frac{\pi}{9}\cot(\pi\zeta_1). \quad (40)$$

Obviously, similar transformation for models (ii) and (iii) can be made for any number of bubbles and, thus, one can conclude that in the framework of these models and in view of (38), the relaxation time grows with the relative length of the ring as l^2.

In the case of three bubbles, all the models lead to systems of two simultaneous autonomous ordinary differential equations. For the nearest-neighbor interaction, model (i), using the reflection method, we obtain

$$\begin{aligned}\frac{dl_1}{dt} &= \Phi_1^{(i)}(l_1, l_2, l-l_1-l_2)\\ &= \frac{1}{18}\left(\frac{2}{l_1} - \frac{1}{l_2} - \frac{1}{l-l_1-l_2} + \frac{1}{l_1 l_2} - \frac{2}{l_2(l-l_1-l_2)}\right.\\ &\quad \left. + \frac{1}{l_1(l-l_1-l_2)} + \frac{9}{5l_2^2} - \frac{18}{5l_1^2} + \frac{9}{5(l-l_1-l_2)^2}\right),\end{aligned}$$

$$\begin{aligned}\frac{dl_2}{dt} &= \Phi_2^{(i)}(l_1, l_2, l-l_1-l_2)\\ &= \frac{1}{18}\left(\frac{2}{l_2} - \frac{1}{l_1} - \frac{1}{l-l_1-l_2} + \frac{1}{l_1 l_2} - \frac{2}{l_1(l-l_1-l_2)}\right.\\ &\quad \left. + \frac{1}{l_2(l-l_1-l_2)} + \frac{9}{5l_1^2} - \frac{18}{5l_2^2} + \frac{9}{5(l-l_1-l_2)^2}\right).\end{aligned} \quad (41)$$

For the pairwise interaction model (ii), the equations are

$$\begin{aligned}\frac{dl_1}{dt} &= \frac{1}{18}\left(\frac{2}{l_1} - \frac{2}{l-l_1} - \frac{1}{l_2} + \frac{1}{l-l_2}\right.\\ &\quad \left. + \frac{1}{l_1+l_2} - \frac{1}{l-l_1-l_2}\right),\\ \frac{dl_2}{dt} &= \frac{1}{18}\left(\frac{2}{l_2} - \frac{2}{l-l_2} - \frac{1}{l_1}\right.\\ &\quad \left. + \frac{1}{l-l_1} + \frac{1}{l_1+l_2} - \frac{1}{l-l_1-l_2}\right),\end{aligned} \quad (42)$$

and for the periodic model (iii), the form is

$$\begin{aligned}\frac{dl_1}{dt} &= \frac{\pi}{18l}\left[2\cot\left(\frac{\pi l_1}{l}\right) - \cot\left(\frac{\pi l_2}{l}\right)\right.\\ &\quad \left. + \cot\left(\frac{\pi(l_1+l_2)}{l}\right)\right],\\ \frac{dl_2}{dt} &= \frac{\pi}{18l}\left[2\cot\left(\frac{\pi l_2}{l}\right) - \cot\left(\frac{\pi l_1}{l}\right)\right.\\ &\quad \left. + \cot\left(\frac{\pi(l_1+l_2)}{l}\right)\right].\end{aligned} \quad (43)$$

It is easy to see that in each of the systems (41), (42), or (43), if $l_1 = l_2$ at some initial moment, then $dl_1/dt = dl_2/dt$ and, hence, $l_1 = l_2$ at any further time. An immediate corollary is that if $l_1(0) > l_2(0)$, then $l_1(t) > l_2(t) \forall t > 0$. The same applies to the pairs $l_1, l_3 = l - l_1 - l_2$ and $l_2, l_3 = l - l_1 - l_2$. Hence, the initially shortest separation remains the shortest, and the initially longest remains the longest.

It is interesting to see a phase plane (l_1, l_2) corresponding to systems (41), (42), and (43). Note that only the domain $l_1 > 2, l_2 > 2, l_1 + l_2 < l - 2$ corresponds to separate bubbles and, thus, is physically relevant. In Fig. 7 the trajectories corresponding to models (i) and (ii) are shown by solid and dotted lines, respectively. Trajectories corresponding to model (iii) are visibly indistinguishable from the dotted lines. The phase plane (l_1, l_2) has a singular point $l_1 = l_2 = l/3$ and three singular lines (trajectories), $l_2 = l_1 = l/3$, $l_2 = l - 2l_1$, and $l_2 = (l - l_1)/2$, which intersect at the singular point and divide the phase plane into six subdomains, as shown in Fig. 7. Any trajectory that starts inside one of these subdomains remains there at any moment of time. In Fig. 7, it is also evident that the shortest separation distance approaches the equilibrium value $l/3$ monotonically and no overshooting takes place. Similarly, the longest separation monotonically decreases and exhibits no undershooting. However, for certain initial conditions, the third separation exhibit nonmonotonic behavior and undershooting of the equilibrium value denoted by the dashed lines.

For the particular solutions along the singular line $l_1 = l_2$, the systems (41), (42), and (43) reduce finally to

$$\frac{dl_1}{dt} = \Phi_1^{(i)}(l_1, l_1, l - 2l_1) = \frac{1}{18}\left(\frac{1}{l_1} - \frac{1}{l - 2l_1}\right)\left(1 - \frac{4}{5l_1} - \frac{9}{5}\frac{1}{l - 2l_1}\right), \quad (44)$$

$$\frac{dl_1}{dt} = \frac{1}{18}\left(\frac{3}{l_1} - \frac{1}{l - l_1} - \frac{1}{l - 2l_1}\right), \quad (45)$$

and

$$\frac{dl_1}{dt} = \frac{\pi}{18l}\left[\cot\left(\frac{\pi l_1}{l}\right) + \cot\left(\frac{2\pi l_1}{l}\right)\right]. \quad (46)$$

The analytical integration of Eq. (44) provides

$$t = 2l_1(3l_1 - l) - \frac{6}{5}l_1 + \frac{9}{50}\frac{\ln|4l - 5ll_1 + l_1 + 10{l_1}^2|}{5l - 39}(565l - 13) - \frac{10l^3}{3}\frac{\ln|3l_1 - l|}{5l - 39} - \tanh^{-1}\left(\frac{20l_1 - 5l + 1}{\sqrt{25l^2 - 170l + 1}}\right)\frac{9}{\sqrt{25l^2 - 170l + 1}}\frac{(1225l^2 - 1670l + 13)}{25(5l - 39)} - h_1(0), \quad (47)$$

where $h_1(0)$ is given by

$$h_1(0) = 2l_1(0)(3l_1(0) - l) - \frac{6}{5}l_1(0) + \frac{9}{50}\frac{\ln|4l - 5ll_1(0) + l_1(0) + 10l_1(0)^2|}{5l - 39}(565l - 13) - \tanh^{-1}\left[\frac{20l_1(0) - 5l + 1}{\sqrt{25l^2 - 170l + 1}}\right]\frac{9}{\sqrt{25l^2 - 170l + 1}}\frac{(1225l^2 - 1670l + 13)}{25(5l - 39)} - \frac{10l^3}{3}\frac{\ln|3l_1(0) - l|}{5l - 39}.$$

Equation (45) can be integrated to yield

$$t = 3l_1^2 - \frac{5}{2}ll_1 - 3l_1^2(0) + \frac{5}{2}ll_1(0) - \frac{27}{40}\ln\left|\frac{4l_1 - 3l}{4l_1(0) - 3l}\right| - \frac{8}{15}\ln\left|\frac{3l_1 - l}{3l_1(0) - l}\right|, \quad (48)$$

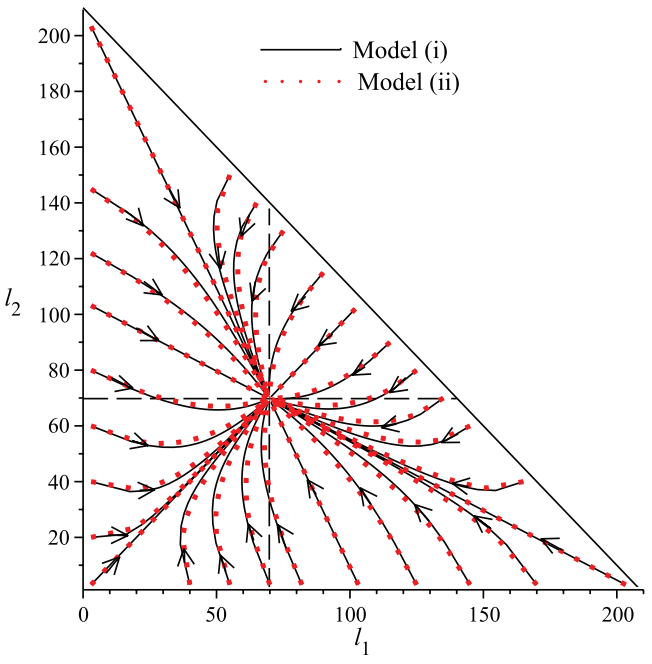

FIG. 7. (Color online) Phase planes: Trajectories calculated by the systems (41) and (42) are shown by solid and dotted lines, respectively, for the streamline length $l = 66.67\pi$.

and the analytical solution of (46) is

$$l_1(t) = \frac{l}{2\pi}\arccos\left\{\frac{[2\cos(2\pi l_1(0)) + 1]\exp\left(-\frac{2\pi^2}{9l^2}t\right) - 1}{2}\right\}. \quad (49)$$

Similar analytical expressions can be obtained for the particular cases $l_2 = l - 2l_1$ and $l_2 = (l - l_1)/2$.

Two other examples of the time evolution of separation distances in three bubbles case with $l = 66.67\pi$, obtained via numerical simulation of (41), (42), and (43), are given in Fig. 8. Solid, dashed, and dashed-dotted lines are computed making use of models (i), (ii), and (iii), respectively. In Figs. 8(a), 8(c), and 8(e) the evolution curves are computed for the initial conditions, $l_1(0) = 3$, $l_2(0) = 65$, while in Figs. 8(b), 8(d), and 8(f) the initial conditions are $l_1(0) = 3$, $l_2(0) = 80$. Evolution of the shortest separation is depicted in Figs. 8(a) and 8(b) and the evolution of the longest one is shown in Figs. 8(e) and 8(f). Here, again, in all the cases the approach to equilibrium of the shortest and longest separations are monotonic and exhibit no overshooting or undershooting. The intermediate separation distance, however, is typically nonmonotonic and can actually undershoot the equilibrium separation distance [see Fig. 8(d)] as is also evident in the phase plane (Fig. 7). One can see that the three models give qualitatively similar behavior of the evolution of the separation distances. However, as can be anticipated, the relaxation time according to the nearest-neighbors interaction model is higher than that those computed according to the other two models.

According to the nearest-neighbors interaction model (i), the evolution of separation distances in cases of more than

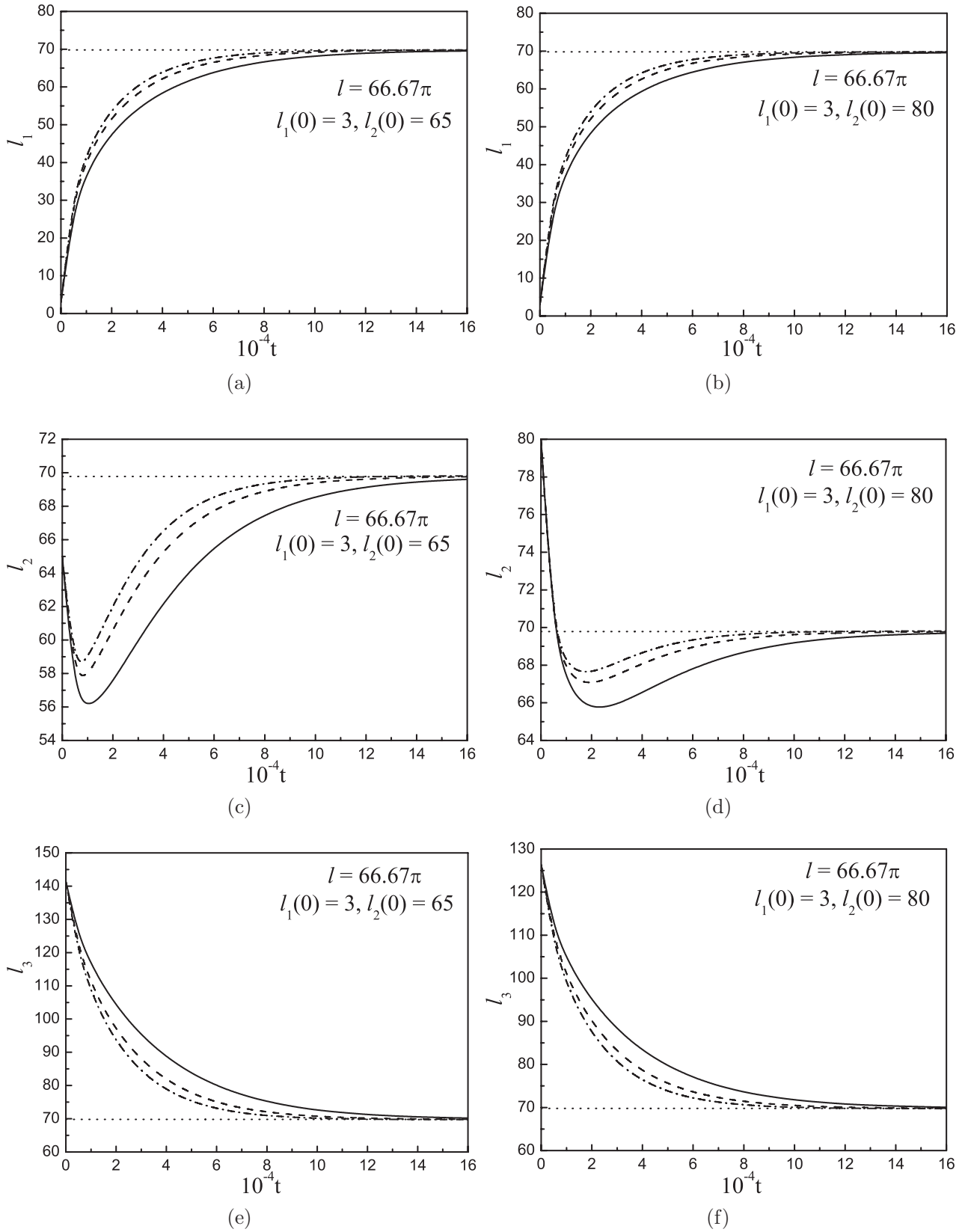

FIG. 8. Examples of the time evolution of separation distances among three bubbles: (a) and (b) correspond to the shortest, (c) and (d) to the intermediate, (e) and (f) to the longest separation distances.

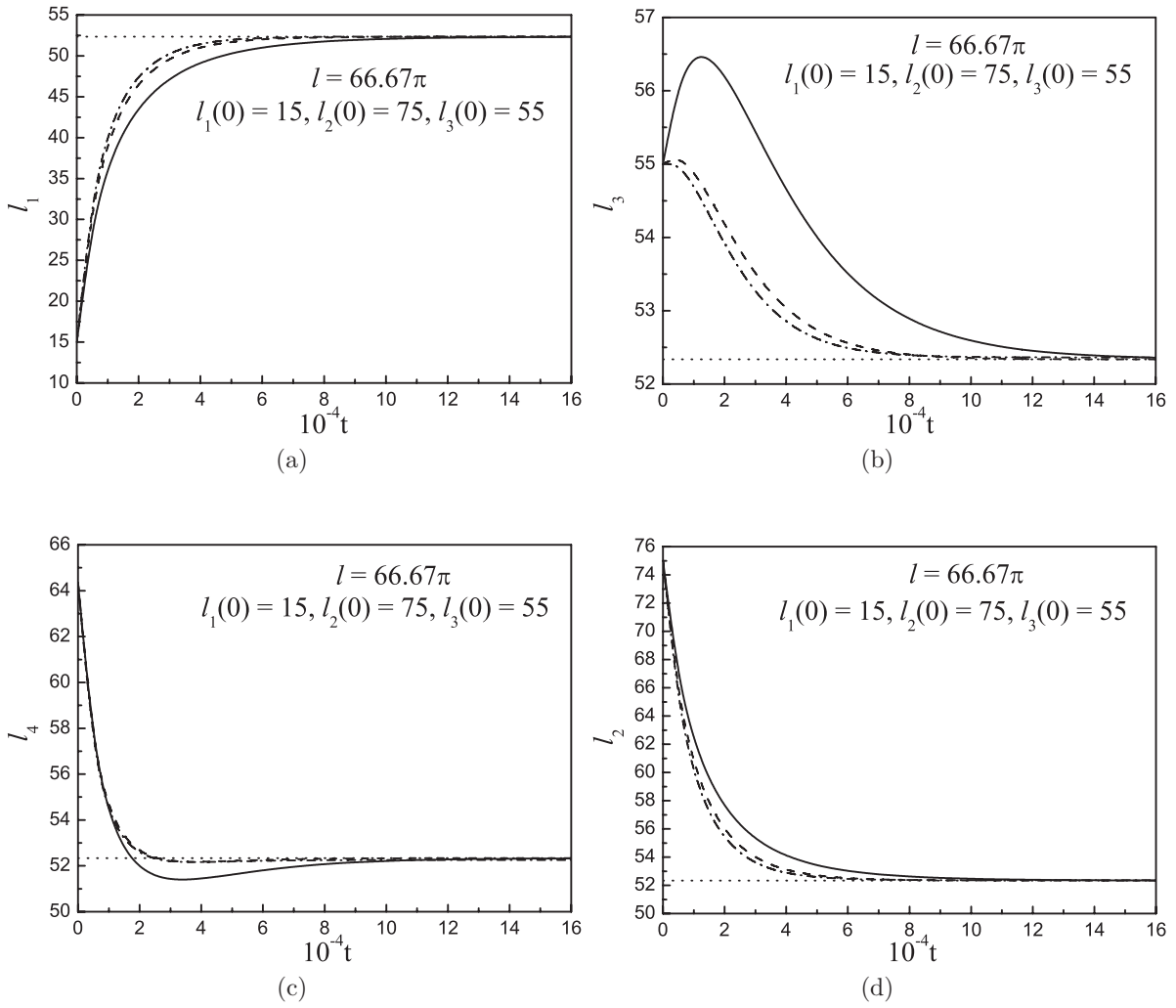

FIG. 9. Examples of the time evolution of separation distances among four bubbles: (a) and (d) correspond to minimal and maximal separation distances, respectively. (b) and (c) correspond to initial intermediate separation distances.

three bubbles is governed by

$$\frac{dl_n}{dt} = \Phi_n\left(l_1,\ldots,l_{N-1},l-\sum_{k=1}^{N-1} l_k\right) = \frac{1}{18}\left(\frac{2}{l_n}-\frac{1}{l_{n-1}}-\frac{1}{l_{n+1}}-\frac{1}{l_{n-2}l_{n-1}}+\frac{1}{l_{n-1}l_n}+\frac{1}{l_nl_{n+1}} - \frac{1}{l_{n+1}l_{n+2}}+\frac{9}{5l_{n-1}^2}-\frac{18}{5l_n^2}+\frac{9}{5l_{n+1}^2}\right), \quad n = 1,\ldots,N-1, \tag{50}$$

where $l_{-1} = l_{N-1}, l_{N+1} = l_1$ and $l_0 = l_N = l - \sum_{k=1}^{N-1} l_k$. Similar expressions corresponding to models (ii) and (iii) follow from Eqs. (29) and (31).

In the case of four bubbles, if at some moment there are two pairs of equal adjacent intervals between the bubbles, say $l_1 = l_2$ while $l_3 = l_4 = (l - 2l_1)/2$ at some moment, then $dl_1/dt = dl_2/dt$ and $dl_3/dt = dl_4/dt$ and, hence, $l_1 = l_2$ and $l_3 = l_4 = (l - 2l_1)/2$ at any time. In this case, again, system (50) is reduced to a single ordinary differential equation on l_1 that can be integrated analytically. This applies to all three models.

An example of the evolution of separation distances in the case of four bubbles having unequal separations is presented in Fig. 9, where $l = 66.67\pi$, $l_1(0) = 15$, $l_2(0) = 75$, $l_3(0) = 55$. Solid, dashed, and dashed-dotted lines are computed making use of models (i), (ii), and (iii), respectively. Minimal and maximal separation distances among four bubbles are presented in Figs. 9(a) and 9(d), respectively, while the intermediate separations are shown in Figs. 9(b) and 9(c). Here in all the cases, the approach to equilibrium of the shortest and longest separations are monotonic and exhibit no overshooting or undershooting phenomena. However, the intermediate separation distance may undershoot the equilibrium separation distance as depicted in Figs. 9(b) and 9(c). As in the case of three bubbles, all three models show qualitatively similar dynamics of the bubbles, with the longest relaxation time corresponding to model (i).

B. Experimental results

An experimental study of the interaction of air bubbles in a mineral oil, captured by steady Taylor vortices in a Couette device, was performed in a setup that consists of a stationary outer cylinder of radius $R_{out} = 3.2$ cm and a concentric rotating inner cylinder of radius $R_{in} = 2$ cm, which provided a uniform gap width of 1.2 cm. A microsyringe pump attached to a teflon microtube drives air through a needle in order to generate uniform bubbles. The diameter of the bubbles was determined by the volume of the injected air and, in these experiments, was of $O(1$ mm). More details about the experimental setup and procedure can be found in Byk *et al.* [4].

It was demonstrated that the dynamics of the bubbles exhibit two different time scales: The short one (of the order of 1 min) is the time required for a bubble to be trapped by a vortex, preventing it from rising due to buoyancy. The redistribution of the bubbles along the center streamline of the vortex, that is, of the primary interest of the current research, takes much longer [$O(10$–100 min)], especially for a low number of injected bubbles. At a certain range of rotation velocity, during the longer time scale, equal-size bubbles are repulsed from each other and eventually assume an ordered ring with equal separation distances among all neighbors. The equilibrium configurations for various numbers of bubbles were shown in Fig. 1. The bubbles in the ring move with equal velocities. This quasistationary structure exists for a long time and appears to be stable.

Several results depicting the evolution of an arbitrary initial distribution to the established uniform ring, depending on the number of injected bubbles, together with evolution predicted by the theoretical models are presented in Figs. 10–12. The dynamics follow the evolution of the initial minimal separation distance among bubbles which is the most remote from the equilibrium separation at all time.

In Figs. 10(a) and 11(a), the measured minimum separation distance between bubbles of radii $a = 0.78$ mm in a fluid of viscosity $\mu = 30$ cp and density $\rho = 0.88$ g/cm^3 is plotted versus time for the cases of three and four bubbles, respectively. The separation was measured along the center streamline. The angular velocity of the inner cylinder in these experiments was $\Omega = 396$ rpm corresponding to bubble Reynolds number $\mathrm{Re} = 2\pi\rho\Omega R_{in}a^2/\mu(R_{out} - R_{in}) \sim 1.23$ in the shear flow.

The three overlapping curves in Figs. 10(a) and 11(a) correspond to different experimental runs under the same experimental conditions and, thus, demonstrate that the large-time-scale behavior is reproduced for different arbitrary initial conditions. One can see that, after a relatively short period of nonmonotonic behavior [negative time in Figs. 10(a) and 11(a)] varying from run to run, which probably depends on the initial location of the bubbles in the vortex, the curves merge to a single monotonically growing one that tends to the value corresponding to the equilibrium symmetric distribution of bubbles in the ring. The higher the number of bubbles in the ring, the shorter the relaxation time. This leads to the assumption that the interaction of the bubbles results in some repulsive force, decaying with the separation distance, which is in a qualitative agreement with characteristics of the inertia-induced force calculated in the previous section.

The comparison of the experimental observations and the theoretical predictions for three and four bubbles is presented

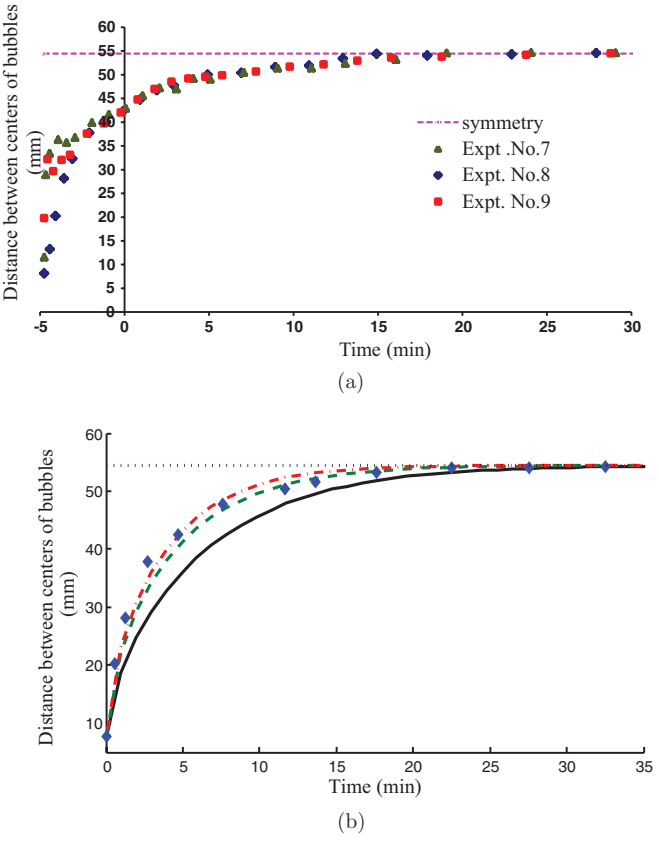

FIG. 10. (Color online) Evolution of minimum separation distance among three bubbles with radii $a = 0.78$ mm in a fluid having viscosity $\mu = 30$ cp, density $\rho = 0.88$ g/cm^3, and angular velocity $\Omega = 396$ rpm. (a) Various markers in the figure correspond to various experimental runs. (b) Markers correspond to experiment 8. Solid, dashed, and dashed-dotted lines are computed via models (i), (ii), and (iii), respectively.

in Figs. 10(b) and 11(b), respectively. Markers in these figures correspond to experiments 8 and 12, respectively. Solid, dashed, and dashed-dotted lines are computed via models (i), (ii), and (iii), respectively. To translate the dimensionless theoretical results into dimensional ones, we take into account that the length and time were scaled by the radius of the bubble a and by $1/(\mathrm{Re}G)$, respectively, where $1/G = (R_{out} - R_{in})/2\pi\Omega R_{in} \sim 2.4 \times 10^{-4}$ min. Note that the time scale for the evolution of the bubbles distribution is related to the above by a factor of $(L/a)^2$ [see also Eqs. (39) and (40)], L being a typical dimensional translation distance. In the case of three bubbles, computations presented in Fig. 10(b) were performed for the initial conditions $l_1(0) = l_2(0) = 10$, while for the four-bubble case presented in Fig. 11(b), the initial conditions were taken as $l_1(0) = 3$, $l_2(0) = l_3(0) = 45$. A variation of the initial conditions for l_2 and l_3 show that the dynamics of evolution of the shortest separation distance, l_1, is relatively insensitive to the former values. One can see that in the cases of three and four bubbles all three models provide similar results that qualitatively agree with the experimental observations. Model (i) evidently overestimates the relaxation time compared to the experimental observation, while the other two model's results are remarkably close to the experiment.

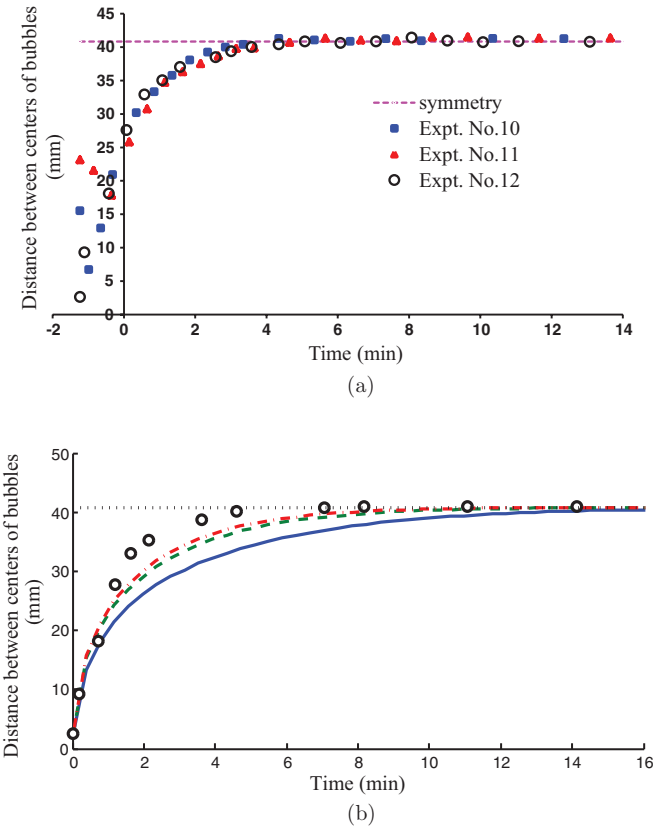

FIG. 11. (Color online) Evolution of minimum separation distance between four bubbles with radii $a = 0.78$ mm in a fluid having viscosity $\mu = 30$ cp, density $\rho = 0.88$ g/cm^3, and angular velocity $\Omega = 396$ rpm. (a) Various markers in the figure correspond to various experimental runs (Byk *et al*. [4]). (b) Markers correspond to experiment 12. Solid, dashed, and dashed-dotted lines are computed via models (i), (ii), and (iii), respectively

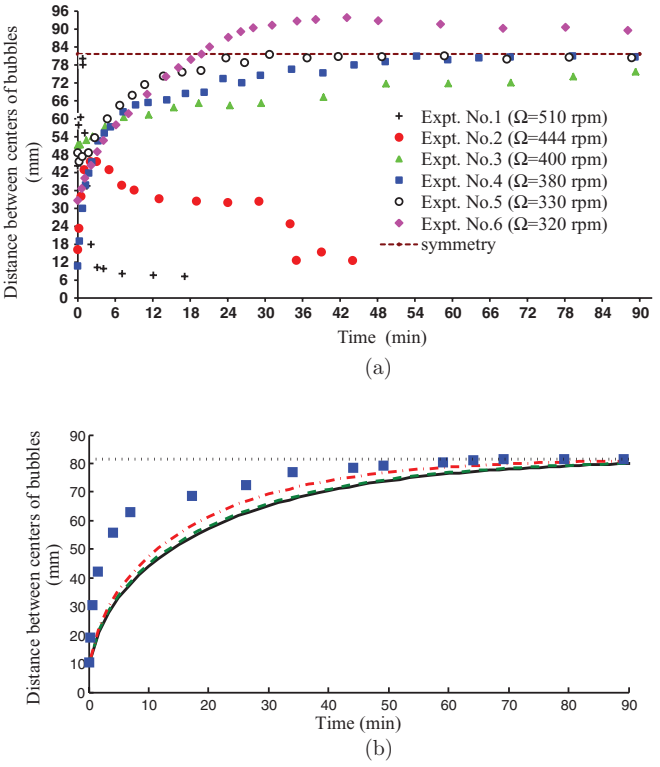

FIG. 12. (Color online) Evolution of the initial minimum separation distance between two bubbles with radii $a = 0.62$ mm in a fluid having viscosity $\mu = 30$ cp and density $\rho = 0.88$ g/cm^3. (a) Various markers are measured in the experiments with various angular velocities. (b) Markers correspond to experiment 4. Solid, dashed, and dashed-dotted lines are computed via models (i), (ii), and (iii), respectively.

The dynamics of two bubbles in viscous fluid in a Couette device at various values of velocity of rotation is illustrated in Fig. 12(a), where we follow the evolution of a chosen (initially minimal) separation. The Reynolds numbers at the bubble scale in these experiments vary from 0.63 to 1.0, thus, being again of $\leqslant O(1)$.

A comparison of the experimental observations and the theoretical predictions for two bubbles is presented in Fig. 12(b). Markers in this figure correspond to experiment 4, while solid, dashed, and dashed-dotted lines are computed via models (i), (ii), and (iii), respectively, with initial condition $l_1 = 10$ [the results obtained via model (i) in this case are almost indistinguishable from those by model (ii) in view of Eqs. (32) and (33)]. To translate the dimensionless results we take into account that the length and time were scaled by the radius of the bubble a and by $1/(\mathrm{Re}G)$, respectively, where $1/G = (R_{\mathrm{out}} - R_{\mathrm{in}})/2\pi\Omega R_{\mathrm{in}} \sim 2.5 \times 10^{-4}$ min.

Here, again, a good agreement of experimental and theoretical results is observed, especially at the advanced stages of the process. However, several effects observed in the experiments are not reflected by the theoretical models. The experimental study suggests that for the two-bubble case the relaxation time increases with the growth of the angular velocity. It also reports that at high-enough angular velocity the repulsive nature of the force may reverse and the bubbles would tend to be attracted to each other and eventually coalesce [experiments 1 and 2 in Fig. 12(a)]. Another interesting result obtained for the two-bubble case is that the evolution of the separation distance may not be monotonic (experiments 4 and 5), and an overshoot of the equilibrium separation is observed (experiment 6). These effects may be due to the fact that when the bubbles are injected into the Taylor vortices they approach the center streamline with a different pace, particularly for different G. In the theoretical analysis the bubbles are assumed on the same streamline and, therefore, an overshoot in equilibrium separation or reversal of the bubble motion are not predicted. Our hypothesis is that these complicated types of behavior are associated with bubbles positioned on different streamlines having different angular velocity. Such a deviation from the middle streamline may be caused by gravitational effect or lateral departure due to increased inertia at relatively lower or higher angular velocity, respectively.

IV. CONCLUSIONS

In this paper, we used the reciprocal theorem to calculate the inertia-induced forces on two identical spherical bubbles in a simple shear flow at a small but finite Reynolds number. This force was shown to be of a repulsive nature and was

further employed to model the dynamics of air bubbles injected into a viscous fluid sheared in a Couette device that experiences the first shear flow instability where the bubbles are trapped inside a stable Taylor vortex.

Three simplified models of such dynamics are suggested: The first assumes that each bubble interacts solely with its nearest neighbors, the second takes into account pair-wise interactions among all the bubbles in the ring, and the third one models the ring by a periodic line of bubbles. We hypothesize that the experimentally observed ordering of the bubbles is due to their inertial interaction in a primary shear flow. The application of the models results in systems of ordinary differential equations describing the evolution of the separations among the bubbles.

It was shown that, according to all of the three suggested models, the inertial interaction among the bubbles in the primary shear flow drives them away from each other and, as a result, equal-size bubbles eventually assume an ordered string with equal separation distances among all neighbors. The relaxation time decreases with the growth of the number of the bubbles.

We report also on experiments showing the dynamic evolution of minimal separation distance for various numbers of bubbles and compare this to the results of computations. The Reynolds numbers in these experiments were of the order 1, while the developed theory assumes small values of Re. Nevertheless, the results computed according to all the models are in good agreement with the experimental observations, i.e., they describe the main effect of approaching the equilibrium position and provide a good measure of the evolution relaxation time. The nearest-neighbors interaction model overestimates the relaxation time, especially with the relatively high number of bubbles in the ring. The results of the other two models are very close to each other and reproduce the experimental dynamics of the minimal separation distance remarkably good. However, neither the overshooting of the equilibrium separation, nor the reversal of the effect that were observed in several experimental runs at various rotation velocities with two bubbles, is reproduced. Our models predict interesting nonmonotonic evolution of separation distances for cases involving more than two bubbles that was not reported in the experimental study, which focused on the minimum separation distance.

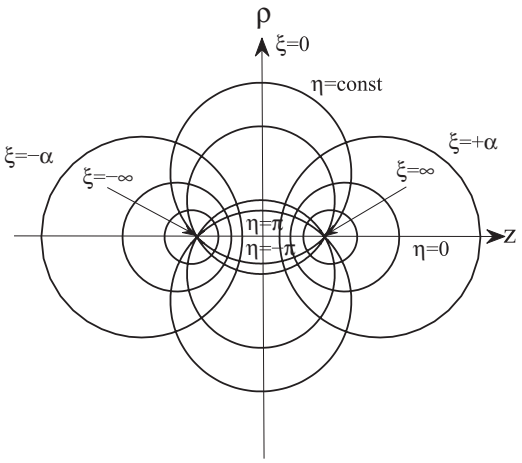

FIG. 13. Schematics of bispherical coordinate system.

ACKNOWLEDGMENTS

The work was supported by Israel Science Foundation (Grant No. ISF/668.11). O.M.L. acknowledges the support of the Israel Ministry of Immigrant Absorption. J.P. acknowledges partial support by a fellowship from Israel Council for Higher Education. The authors are grateful to the anonymous referees for their valuable comments and suggestions, which helped improve the quality of the paper.

APPENDIX: BISPHERICAL COORDINATES

Consider the bispherical coordinate system connected with the two bubbles of radii unity as shown in Fig. 13 and linked with the cylindrical system (ρ,z,ϕ) by the following relation:

$$\rho = \frac{c\sin\eta}{\cosh\xi - \cos\eta}, \quad z = \frac{c\sinh\xi}{\cosh\xi - \cos\eta}, \quad \phi = \phi, \qquad \text{(A1)}$$

where $-\infty < \xi < \infty$, $0 \leqslant \eta \leqslant \pi$, and $0 \leqslant \phi \leqslant 2\pi$ and c is related to the distance between the centers of bubbles and d by $c = \frac{1}{2}\sqrt{d^2-4}$. The interface of bubble 1 is described by the coordinate surface $\xi = \alpha > 0$ and the interface of bubble 2 corresponds to $\xi = -\alpha > 0$, where α is a constant given by $\alpha = \sinh^{-1}(c)$.

The link provided by Eq. (A1) between bispherical and cylindrical coordinates allows one to derive the solution to Laplace equation in terms of the former from the latter. The dimensionless Stokes equations given in (9) in component form in cylindrical coordinates together with mass conservation are

$$\left(\nabla^2 - \frac{1}{\rho^2}\right)v_\rho^0 - \frac{2}{\rho^2}\frac{\partial v_\phi^0}{\partial\phi} = \frac{\partial p^0}{\partial\rho}, \quad \left(\nabla^2 - \frac{1}{\rho^2}\right)v_\phi^0 + \frac{2}{\rho^2}\frac{\partial v_\rho^0}{\partial\phi} = \frac{1}{\rho}\frac{\partial p^0}{\partial\phi}, \quad \nabla^2 v_z^0 = \frac{\partial p^0}{\partial z}, \quad \frac{\partial v_\rho^0}{\partial\rho} + \frac{1}{\rho}v_\rho^0 + \frac{1}{\rho}\frac{\partial v_\phi^0}{\partial\phi} + \frac{\partial v_z^0}{\partial z} = 0. \qquad \text{(A2)}$$

Following Lin, Lee, and Sather [20], the pressure and velocity components are of the form

$$p^0 = \frac{1}{c}\sum_{n=1}^{\infty}(\cosh\xi - \cos\eta)^{1/2}\left[A_{-1n}^0\cosh\left(n+\frac{1}{2}\right)\xi + B_{-1n}^0\sinh\left(n+\frac{1}{2}\right)\xi\right]P_n^1(\cos\eta)\cos\phi, \qquad \text{(A3)}$$

$$v_\rho^0 = \frac{1}{2}(\cosh\xi - \cos\eta)^{1/2}\left[\frac{\sin\eta}{\cosh\xi - \cos\eta}\sum_{n=1}^{\infty} B_{-1n}^0 \sinh\left(n+\frac{1}{2}\right)\xi P_n^1(\cos\eta) + \sum_{n=0}^{\infty} B_{-1n}^{-1}\sinh\left(n+\frac{1}{2}\right)\xi P_n(\cos\eta) + \sum_{n=2}^{\infty} B_{-1n}^1 \sinh\left(n+\frac{1}{2}\right)\xi P_n^2(\cos\eta)\right]\cos\phi, \tag{A4}$$

$$v_z^0 = \frac{1}{2}(\cosh\xi - \cos\eta)^{1/2}\left[\frac{\sinh\xi}{\cosh\xi - \cos\eta}\sum_{n=1}^{\infty} B_{-1n}^0 \sinh\left(n+\frac{1}{2}\right)\xi P_n^1(\cos\eta) + 2\sum_{n=1}^{\infty} A_{-1n}^0 \cosh\left(n+\frac{1}{2}\right)\xi P_n^1(\cos\eta)\right]\cos\phi, \tag{A5}$$

$$v_\phi^0 = -\frac{1}{2}(\cosh\xi - \cos\eta)^{1/2}\left[\sum_{n=0}^{\infty} B_{-1n}^{-1}\sinh\left(n+\frac{1}{2}\right)\xi P_n(\cos\eta) - \sum_{n=2}^{\infty} B_{-1n}^1 \sinh\left(n+\frac{1}{2}\right)\xi P_n^2(\cos\eta)\right]\sin\phi, \tag{A6}$$

where A_{1n}^0, B_{-1n}^0, B_{-1n}^{-1}, and B_{-1n}^1 are unknown constants to be determined from the boundary conditions and $P_n = P_n^0$, P_n^1, and P_n^2 are associated Legendre polynomials of degree n and order 0, 1, 2, respectively. In (A3)–(A6) symmetry and antisymmetry of the flow field with respect to ξ were taken into account.

In order to determine the unknown constants A_{1n}^0, B_{-1n}^0, B_{-1n}^{-1}, and B_{-1n}^1, the expressions (A3)–(A6) are substituted into the equation of continuity and boundary conditions (4) and (6). The relations among associated Legendre polynomials then are used to express both sides of the obtained equations in terms of P_n^1. These equations are, thus, reduced to an infinite system of linear algebraic equations on the coefficients

$$\begin{aligned}&5B_{-1n}^0 - (n-1)B_{-1n-1}^0 + (n+2)B_{-1n+1}^0 - 2B_{-1n}^{-1} + B_{-1n-1}^{-1} + B_{-1n+1}^{-1} + 2(n-1)(n+2)B_{-1n}^1 - (n-1)(n-2)B_{-1n-1}^1\\ &-(n+2)(n+3)B_{-1n+1}^1 + 2(2n+1)A_{-1n}^0 - 2(n-1)A_{-1n-1}^0 - 2A_{-1n+1}^0 = 0, \quad n = 1,\ldots,\infty.\end{aligned} \tag{A7}$$

$$\begin{aligned}&\frac{(n-1)}{(2n-1)}B_{-1n-1}^0\sinh\left(n-\frac{1}{2}\right)\alpha + \frac{(n+2)}{(2n+3)}B_{-1n+1}^0\sinh\left(n+\frac{3}{2}\right)\alpha - \frac{1}{(2n-1)}B_{-1n-1}^{-1}\sinh\left(n-\frac{1}{2}\right)\alpha\\ &+\frac{1}{(2n+3)}B_{-1n+1}^{-1}\sinh\left(n+\frac{3}{2}\right)\alpha\frac{(n-1)(n-2)}{(2n-1)}B_{-1n-1}^1\sinh\left(n-\frac{1}{2}\right)\alpha - \frac{(n+2)(n+3)}{(2n+3)}B_{-1n+1}^1\sinh\left(n+\frac{3}{2}\right)\alpha\\ &-2A_{-1n}^0\mathrm{cosech}\alpha\cosh\left(n+\frac{1}{2}\right)\alpha + \frac{2(n-1)}{(2n-1)}A_{-1n-1}^0\coth\alpha\cosh\left(n-\frac{1}{2}\right)\alpha\\ &+\frac{2(n+2)}{(2n+3)}A_{-1n+1}^0\coth\alpha\cosh\left(n+\frac{3}{2}\right)\alpha = \frac{4\sqrt{2}c\coth\alpha}{(2n+3)(2n-1)}\left\{(n+2)(2n-1)\exp\left[-\left(n+\frac{3}{2}\right)\right]\alpha\right.\\ &\left.+(n-1)(2n+3)\exp\left[-\left(n-\frac{1}{2}\right)\right]\alpha - (2n+3)(2n-1)\mathrm{sech}\alpha\exp\left[-\left(n+\frac{1}{2}\right)\right]\alpha\right\}, \quad n = 1,\ldots,\infty.\end{aligned} \tag{A8}$$

$$\begin{aligned}&\frac{(n-1)}{(2n-1)}B_{-1n-2}^{-1}\mathrm{cosech}\alpha\cosh\left(n-\frac{3}{2}\right)\alpha + \frac{1}{(2n-1)}h_{-1n-1}^{-1}B_{-1n-1}^{-1}\\ &-\frac{(2n+1)}{(2n+3)(2n-1)}B_{-1n}^{-1}\mathrm{cosech}\alpha\cosh\left(n+\frac{1}{2}\right)\alpha - \frac{1}{(2n+3)}h_{-1n+1}^{-1}B_{-1n+1}^{-1}\\ &+\frac{(n+2)}{(2n+3)}B_{-1n+2}^{-1}\mathrm{cosech}\alpha\cosh\left(n+\frac{5}{2}\right)\alpha - \frac{(n-1)(n-2)(n-3)}{(2n-1)}B_{-1n-2}^1\mathrm{cosech}\alpha\cosh\left(n-\frac{3}{2}\right)\alpha\\ &+\frac{(n-1)(n-2)}{(2n-1)}h_{-1n-1}^1B_{-1n-1}^1 + \frac{3(n-1)(n-2)(2n+1)}{(2n+3)(2n-1)}B_{-1n}^1\mathrm{cosech}\alpha\cosh\left(n+\frac{1}{2}\right)\alpha\\ &-\frac{(n+2)(n+3)}{(2n+3)}h_{-1n+1}^1B_{-1n+1}^1 + \frac{(n+2)(n+3)(n+4)}{(2n+3)}B_{-1n+2}^1\mathrm{cosech}\alpha\cosh\left(n+\frac{5}{2}\right)\alpha = 0,\end{aligned} \tag{A9}$$

where

$$h^{-1}_{-1n} = \left[3\sinh\left(n+\frac{1}{2}\right)\alpha - (2n+1)\coth\alpha\cosh\left(n+\frac{1}{2}\right)\alpha\right]$$
$$h^{1}_{-1n} = \left[3\sinh\left(n+\frac{1}{2}\right)\alpha + (2n+1)\coth\alpha\cosh\left(n+\frac{1}{2}\right)\alpha\right], \quad n = 1,\ldots,\infty$$

$$\begin{aligned}
&\frac{(n-1)(n-2)}{2(2n-3)(2n-1)}\left[B^{-1}_{-1n-3} - (n-3)B^{0}_{-1n-3} - (n-3)(n-4)B^{1}_{-1n-3} + 2(n-3)A^{0}_{-1n-3}\right]\\
&\times\left[\sinh\left(n-\frac{5}{2}\right)\alpha - \coth\alpha\cosh\left(n-\frac{5}{2}\right)\alpha\right] + \frac{(n-1)(n-2)}{2(2n-1)(2n-3)}\cosh\alpha\\
&\times\left[(2n-5)\sinh\left(n-\frac{3}{2}\right)\alpha - (2n-3)\coth\alpha\cosh\left(n-\frac{3}{2}\right)\alpha\right]B^{0}_{-1n-2} - \frac{(n-1)}{2(2n-1)(2n+3)(2n-3)}\\
&\times\left[(2n^3-5n^2-6n+18)\sinh\left(n-\frac{1}{2}\right)\alpha + n^2(2n-1)\coth\alpha\cosh\left(n-\frac{1}{2}\right)\alpha\right]B^{0}_{-1n-1}\\
&+\frac{1}{(2n-1)(2n-3)}\cosh\alpha\left[3\sinh\left(n+\frac{1}{2}\right)\alpha + n(n+1)(2n+1)\coth\alpha\cosh\left(n+\frac{1}{2}\right)\alpha\right]B^{0}_{-1n}\\
&+\frac{(n+2)}{2(2n-1)(2n+3)(2n+5)}\left[(2n^3+11n^2+10n-17)\sinh\left(n+\frac{3}{2}\right)\alpha - (n+1)^2(2n+3)\coth\alpha\cosh\left(n+\frac{3}{2}\right)\alpha\right]\\
&\times B^{0}_{-1n+1} - \frac{(n+2)(n+3)}{2(2n+3)(2n+5)}\cosh\alpha\left[(2n+7)\sinh\left(n+\frac{5}{2}\right)\alpha + (2n+5)\coth\alpha\cosh\left(n+\frac{5}{2}\right)\alpha\right]B^{0}_{-1n+2}\\
&+\frac{(n+2)(n+3)}{2(2n+3)(2n+5)}\left[B^{-1}_{-1n+3} + (n+4)B^{0}_{-1n+3} - (n+4)(n+5)B^{1}_{-1n+3} + 2(n+4)A^{0}_{-1n+3}\right]\\
&\times\left[\sinh\left(n+\frac{7}{2}\right)\alpha + \coth\alpha\cosh\left(n+\frac{7}{2}\right)\alpha\right] - \frac{1}{2(2n-1)(2n+3)(2n-3)}\\
&\times\left[(2n^3+5n^2-n-15)\sinh\left(n-\frac{1}{2}\right)\alpha + (5n^2+2n-1)(2n-1)\coth\alpha\cosh\left(n-\frac{1}{2}\right)\alpha\right]B^{-1}_{-1n-1}\\
&-\frac{(n-1)}{2(2n-1)(2n-3)}\left[B^{-1}_{-1n-2} - (n-2)(n-3)B^{1}_{-1n-2}\right]\left[(2n-5)\cosh\alpha\sinh\left(n-\frac{3}{2}\right)\alpha\right.\\
&\left.-(2n-3)\mathrm{cosech}\alpha(1+\cosh^2\alpha)\cosh\left(n-\frac{3}{2}\right)\alpha\right] + \frac{1}{2(2n-1)(2n-3)}\\
&\times\left[(2n+1)^2\sinh\left(n+\frac{1}{2}\right)\alpha + (2n+1)\mathrm{cosech}\alpha(1+\cosh^2\alpha)\cosh\left(n+\frac{1}{2}\right)\alpha\right]B^{-1}_{-1n}\\
&-\frac{1}{2(2n-1)(2n+3)(2n+5)}\left[(2n^3+n^2-5n+11)\sinh\left(n+\frac{3}{2}\right)\alpha\right.\\
&\left.-(2n+3)(5n^2+9n-8)\coth\alpha\cosh\left(n+\frac{3}{2}\right)\alpha\right]B^{-1}_{-1n+1} - \frac{(n+2)}{2(2n+3)(2n+5)}\left[B^{-1}_{-1n+2} - (n+3)(n+4)B^{1}_{-1n+2}\right]\\
&\times\left[(2n+7)\cosh\alpha\sinh\left(n+\frac{5}{2}\right)\alpha + (2n+5)\mathrm{cosech}\alpha(1+\cosh^2\alpha)\cosh\left(n+\frac{5}{2}\right)\alpha\right]\\
&+\frac{(n-1)(n-2)}{2(2n-1)(2n+3)(2n-3)}\left[(2n^3+13n^2-9n-45)\sinh\left(n-\frac{1}{2}\right)\alpha\right.\\
&\left.+(2n-1)(5n^2-3n-18)\coth\alpha\cosh\left(n-\frac{1}{2}\right)\alpha\right]B^{1}_{-1n-1}\\
&-\frac{(n-1)(n+2)}{2(2n-1)(2n+3)}\left[(4n^2+4n-15)\cosh\alpha\sinh\left(n+\frac{1}{2}\right)\alpha - 3(2n+1)\mathrm{cosech}\alpha(1+\cosh^2\alpha)\cosh\left(n+\frac{1}{2}\right)\alpha\right]B^{1}_{-1n}\\
&+\frac{(n+2)(n+3)}{2(2n-1)(2n+3)(2n+5)}\left[(2n^3-7n^2-29n+25)\sinh\left(n+\frac{3}{2}\right)\alpha\right.
\end{aligned}$$

$$
\begin{aligned}
&-(2n+3)(5n^2+13n-10)\coth\alpha\cosh\left(n+\frac{3}{2}\right)\alpha\Big]B^1_{-1n+1}-\frac{(n-1)(n-2)}{(2n-1)(2n-3)}\Big[(2n-3)\cosh\alpha\sinh\left(n-\frac{3}{2}\right)\alpha\\
&-\{(2n-5)\cosh^2\alpha+2(n-1)\}\mathrm{cosech}\alpha\cosh\left(n-\frac{3}{2}\right)\alpha\Big]A^0_{-1n-2}-\frac{(n-1)}{2(2n-1)(2n+3)(2n-3)}\\
&\times\left[n^2(2n-1)\sinh\left(n-\frac{1}{2}\right)\alpha+(10n^3-13n^2-24n+36)\coth\alpha\cosh\left(n-\frac{1}{2}\right)\alpha\right]A^0_{-1n-1}\\
&+\frac{2}{(2n-1)(2n+1)(2n+3)}\Big[n(n+1)(2n+1)^2\cosh\alpha\sinh\left(n+\frac{1}{2}\right)\alpha\\
&+3\{(2n+1)\cosh^2\alpha-(2n^3+3n^2-n-1)\}\mathrm{cosech}\alpha\cosh\left(n+\frac{1}{2}\right)\alpha\Big]A^0_{-1n}\\
&-\frac{(n+2)}{2(2n-1)(2n+3)(2n+5)}\Big[(n+1)^2(2n+3)\sinh\left(n+\frac{3}{2}\right)\alpha\\
&-(10n^3+43n^2+32n-37)\coth\alpha\cosh\left(n+\frac{3}{2}\right)\alpha\Big]A^0_{-1n+1}-\frac{(n+2)(n+3)}{(2n+3)(2n+5)}\\
&\times\left[(2n+5)\cosh\alpha\sinh\left(n+\frac{1}{2}\right)\alpha+\{(2n+7)\cosh^2\alpha+2(n+2)\}\mathrm{cosech}\alpha\cosh\left(n+\frac{1}{2}\right)\alpha\right]A^0_{-1n+2}\\
=\;&4\sqrt{2}c\Big\{(2-\cosh^2\alpha)\exp\left[-\left(n+\frac{1}{2}\right)\right]\alpha+\frac{\left(4n^3+6n^2-4n-3\right)}{(2n+1)(2n+3)(2n-1)}(2\cosh^2\alpha-1)\exp\left[-\left(n+\frac{1}{2}\right)\right]\alpha\\
&-\frac{2(n+2)}{(2n+3)}\cosh\alpha\exp\left[-\left(n+\frac{3}{2}\right)\right]\alpha+\frac{(n+2)(n+3)}{(2n+3)(2n+5)}(2\cosh^2\alpha-1)\exp\left[-\left(n+\frac{5}{2}\right)\right]\alpha\\
&+\frac{(n-1)(n-2)}{(2n-3)(2n-1)}\left(2\cosh^2\alpha-1\right)\exp\left[-\left(n-\frac{3}{2}\right)\right]\alpha-\frac{2(n-1)}{(2n-1)}\cosh\alpha\exp\left[-\left(n-\frac{1}{2}\right)\right]\alpha\Big\},\quad n=1,\ldots,\infty.
\end{aligned}
\tag{A10}
$$

This system is truncated at some large N and is solved numerically using MATLAB. The accuracy is checked by repeating the procedure at $2N$ and comparing the results.

[1] H. Djéridi, J. F. Fave, J. Y. Billard, and D. H. Fruman, Exp. Fluids **26**, 233 (1999).
[2] H. Djéridi, C. Gabillet, and J. Y. Billard, Phys. Fluids **16**, 128 (2004).
[3] R. Deng, C.-H. Wang, and K. A. Smith, Phys. Rev. E **73**, 036306 (2006).
[4] L. Byk, O. M. Lavrenteva, R. Spivak, and A. Nir, Microgravity Sci. Technol. **19**, 78 (2007).
[5] P. G. Saffman, J. Fluid Mech. **22**, 385 (1965).
[6] P. G. Saffman, J. Fluid Mech. **31**, 624 (1968).
[7] J. B. McLaughlin, J. Fluid Mech. **224**, 261 (1991).
[8] D. Legendre and J. Magnaudet, Phys. Fluids **9**, 3572 (1997).
[9] J. B. McLaughlin, J. Fluid Mech. **246**, 249 (1993).
[10] E. S. Asmolov and F. Feuillebois, J. Fluid Mech. **643**, 449 (2010).
[11] C. J. Lin, J. H. Peery, and W. R. Schowalter, J. Fluid Mech. **44**, 1 (1970).
[12] B. P. Ho and L. G. Leal, J. Fluid Mech. **65**, 365 (1974).
[13] G. Subramanian, D. L. Koch, J. Zhang, and C. Yang, J. Fluid Mech. **674**, 307 (2011).
[14] G. Subramanian and D. L. Koch, Phys. Fluids **18**, 073302 (2006).
[15] Y. Rosenstein and A. M. Leshansky, Euro. J. Mech. B/Fluids **31**, 71 (2012).
[16] P. M. Kulkarni and J. F. Morris, J. Fluid Mech. **596**, 413 (2008).
[17] D. R. Mikulencak and J. F. Morris, J. Fluid Mech. **520**, 215 (2004).
[18] P. O. Olapade, R. K. Singh, and K. Sarkar, Phys. Fluids **21**, 063302 (2009).
[19] R. K. Singh and K. Sarkar, Phys. Fluids **21**, 103303 (2009).
[20] C. J. Lin, K. J. Lee, and N. F. Sather, J. Fluid Mech. **43**, 35 (1970).
[21] R. G. Cox, I. Y. Z. Zia, and S. G. Mason, J. Colloid Interface Sci. **27**, 7 (1968).
[22] G. K. Batchelor and J. T. Green, J. Fluid Mech. **56**, 375 (1972).
[23] S. Torza, C. P. Henry, R. G. Cox, and S. G. Mason, J. Colloid Interface Sci. **35**, 529 (1971).
[24] S. Kim and S. J. Karrila, *Microhydrodynamics: Principles and Selected Applications* (Butterworth-Heinemann, London, 2005).
[25] M. Stimson and G. B. Jeffery, Proc. R. Soc. Lond. Ser. A **111**, 110 (1926).
[26] J. Happel and H. Brenner, *Low Reynolds Number Hydrodynamics: With Special Applications to Particulate Media* (Kluwer Academic, Amsterdam, 1983).